CHARACTERIZATION OF PARTICULATE MATTER EMITTED FROM DIESEL ENGINE

Ki-Hyouk CHOI and Isao MOCHIDA,

Institute of Advanced Material Study, Kyushu University, Kasuga-Koen, Kasuga, Fukuoka 816-8580 JAPAN

Introduction

Particulate matters(PM) emitted from mobile and stationary sources threaten public health because PM carries carcinogenic polyaromatic hydrocarbons(PAHs)[1]. As one of the efforts to diminish the PM, several kinds of exhaust treatment system which has been adopted and tested for diesel engine[2]. The most effective aftertreatment system has been thought to be particulate filter which traps and oxidizes PM. Back pressure exerted by the accumulated PM in particulate filter could arise many problems, for example, high fuel consumption. Hence, PM accumulated in the filter should be removed periodically or continuously by thermal or chemical manners. From the practical viewpoint, oxidative regeneration has been regarded as the most effective method to maintain the filter system in high efficiency[3].

Particulate matter is mainly consisted of elemental carbon, adsorbed hydrocarbons and inorganic compounds(sulfates and water, etc.)[4]. it is not easy to remove PM completely from filter systems during whole cycle of diesel car driving since exhaust temperature is not maintained at high enough to oxidize PM[5]. In order to augment the oxidation of PM, NO_2, which is regarded as stronger oxidant than molecular oxygen, could be generated by catalyst and used for PM oxidation.

We investigated the oxidative properties of PM sampled from diesel engine in order to elucidate the governing factors in PM oxidation under practical gas compositions.

Experimental

Particulate Matter Samples. The PM samples used in this study were supplied from Petroleum Energy Center of Japan. Engine operating conditions and SOF contents, which were calculated after Soxhlet extraction by hexane-acetone(1:1), are listed in Table 1.

Table 1. Engine Operating Conditions for PM samples

Sample Name	Mode	Speed	Torque	Sulfur in fuel(ppmS)	SOF content
Sample #1	6	60%	40%	10	17.2%
Sample #2	10	60%	80%	10	22.7%
PL-10	6	60%	40%	10	20.2%
PL-20	10	60%	80%	10	5.5%
PL-30	6	60%	40%	50	14.2%
PL-40	10	60%	80%	50	4.6%

Characterization of PM samples. The oxidative characteristics of PM samples were investigated by thermogravimetric analysis(TGA, Seiko SSC 5200) and temperature-programmed desorption/oxidation (TPD and TPO, Nippon Bel TPD-1-AT) method. The sample weight was regulated in 10 - 20 mg in TGA and 2 - 3mg in TPD/TPO experiments to minimize the gas composition and temperature gradients in sample bed. The total gas flow rate was 200 ml/min and 50 ml/min for TGA and TPD/TPO, respectively. O_2, NO_2 and SO_2 used in this study were balanced in nitrogen and helium for TGA and TPD, respectively. During TPD/TPO experiments gas composition were analyzed by Quadrupole Mass Spectrometer(QMS). X-ray diffractometer(Rigaku, Geigerflex) was used for crystallographic characterization of PM samples.

Results and Discussion

Figure 1 showed X-ray diffractogram of PL-20 and PL-40. Degree of graphitazability calculated from FWHM of 200 peak were calculated at 0.97nm and 1.06 nm, which is similar to that of carbon black[6]. Spherules with diameter of around 25nm could be observed on SEM images of samples.

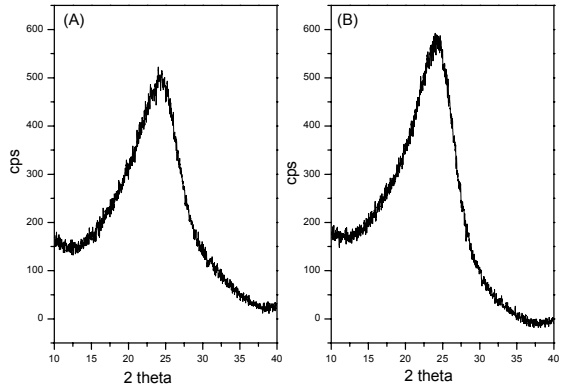

Figure 1. X-ray diffractograms of (A) PL-20 and (B) PL-40.

TGA results of Sample #1 shown in Figure 2 indicates the weight gain under oxidative atmosphere. The sample weights from room temperature to 400 ~ 500 ^oC surpassed those under N2 flow. The weight gain under oxidative atmosphere could be ascribed to the formation of surface complexes between PM and oxidative gases[7]. The presence of NO_2 in O_2 flow facilitated oxidation of PM. However, 7% O_2 showed faster weight loss than under 15% O_2 in the presence of 200ppm NO_2. Furthermore, SO_2 retarded oxidation. These results agreed well with TPO results described below.

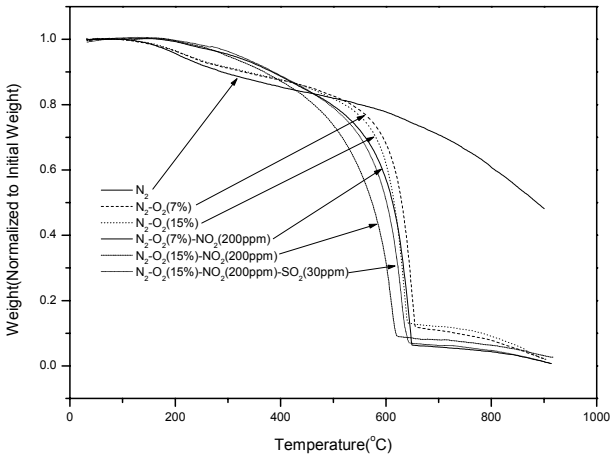

Figure 2. TGA results of Sample #1 under various atmospheres.

TPD under helium flow showed little desorption of CO and CO_2 and TPO under O_2 flow showed main peak at around 600 oC. In contrast to TPO under O_2, CO_2 evolved under NO_2 was small amount and showed broad peak from 100 oC to 900 oC(**Figure 2**). In CO_2 TPO under He-O2(15%) flow, small shoulder could be observed around 350 oC as in **Figure 3**, which could be ascribed to oxidation of hydrocarbon(SOF) and/or soot carbon closely bound to SOF[5, 8, 9].

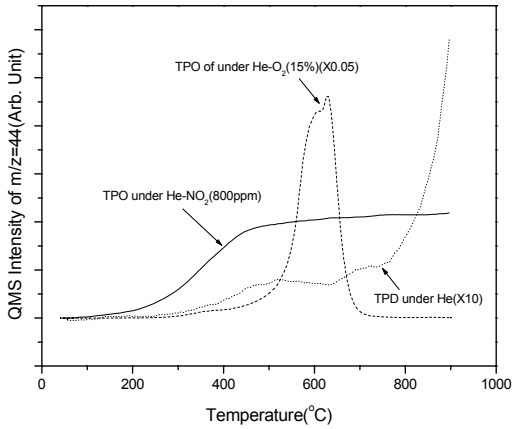

Figure 3. CO_2 TPD spectra under He flow and TPO under He-O_2(15%), He-NO_2(800ppm) of PL-20.

NO_2 addition to He-O_2 flow made CO_2 TPO curves broader than those under He-O_2 as **Figure 4**. Although CO_2 TPO under He-O_2(15%) showed higher evolution rate at low temperature than that under He-O_2(7%), CO_2 evolution under He-O_2(7%)-NO_2(800ppm) started from lower temperature and showed broader band than those under He-O_2(15%)-NO_2(800ppm).

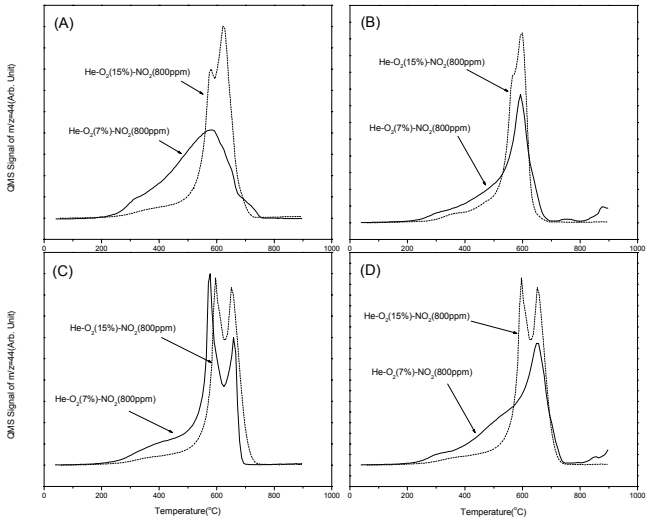

Figure 4. CO_2 TPO spectra under He-O_2(7%)-NO_2(800ppm) and He-O_2(15%)-NO_2(800ppm) of (A) PL-10, (B) PL-20, (C) PL-30, and (D) PL-40.

Taking into account of practical exhaust gas compositions, these results indicates the importance of O_2/NO_2 ratio in PM oxidation. Although the smaller CO_2 evolution at low temperature range under He-O_2(15%)-NO_2(800ppm) than that under He-O_2(7%)-NO_2(800ppm) is hard to be explained, it could be assumed to be originated from the dependency of properties of surface complexes on the gas composition.

The presence of SO_2 retarded oxidation very much as in **Figure 5**.

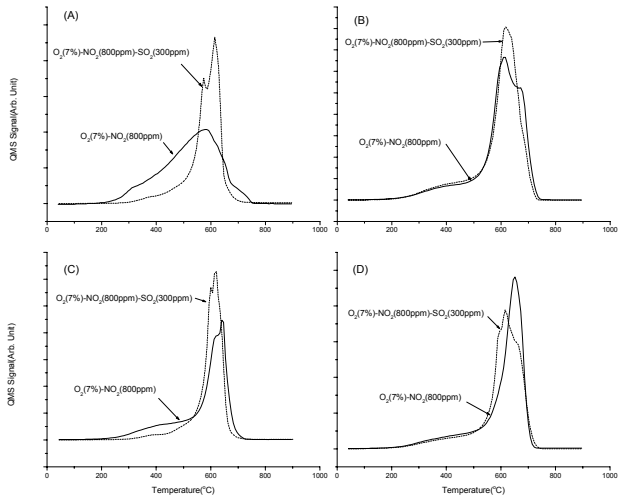

Figure 5. CO_2 TPO spectra under He-O_2(7%)-NO_2(800ppm) and He-O_2(7%)-NO_2(800ppm)-SO_2(300ppm) of (A) PL-10, (B) PL-20, (C) PL-30, and (D) PL-40.

The retardation of oxidation by SO_2 was more pronounced in the low temperature range and larger SOF containing samples. SO_2 have been reported to act as an oxygen trap through oxidizing itself to SO_3, which is strong oxidant[10]. Therefore, adsorbed SO_2 could make oxygen less available to oxidation in the low temperature range and SO_3 formed by the reaction between SO_2 and O_2 could oxidize PM more easily than O_2+NO_2.

Conclusions

The oxidation of particulate matter emitted from diesel engine was dependent on the gas compositions and SOF content of particulate matter. Although NO_2 facilitated oxidation in the co-presence of O_2, it's effect relied on the oxygen content. SO_2 seems to absorb oxygen in the low temperature to oxidize itself to SO_3 and therefore retarded oxidation of particulate matter.

Acknowledgement. This work was supported by the Petroleum Energy Center of Japan.

References

(1) Harrison, R. M.; and Yin, J. *Sci. Total Environ*., **2000**, *249*, 85.
(2) Neeft, J. P. A.; Makkee, M.; Moulijn, J. A. *Fuel Proc. Technol*., **1996**, *47*, 1.
(3) Koltsakis, G. C.; and Stamatelos, A. M. *Prog. Energy Combust. Sci*., **1997**, *23*, 1.
(4) Stein, H. J. *Appl. Catal. B: Environ*., **1996**, *10*, 69.
(5) Kandylas, I. P.; and Stamatelos, A. M. *Ind. Eng. Chem. Res*., **1999**, *38*, 1866.
(6) Hess, W. M. and Herd, C. R. In *Carbon Black*; Donnet, J.-B, Bansal, R. C., Wang, M.-J., Ed: Marcel Dekker, Inc.; New York, 1993; pp.89-174.
(7) Moulijn, J. A.; and Kapteijn, F. *Carbon*, **1995**, *33*, 1155.
(8) Neeft, J. P. A.; Nijhuis, T. X.; Smakman, E.; Makkee. M.; and Moulijn, J. A. *Fuel*, **1997**, 76, 1129.
(9) Zinbo, M.; Skewes, L. M.; Hunter, C. E.; and Schuetzle, D. *Thermochimica Acta*, **1990**, *166*, 267.

COMPARISON OF THE IMPACT OF INTAKE OXYGEN ENRICHMENT AND FUEL OXYGENATION ON DIESEL PARTICULATE EMISSIONS

Juhun Song, Vince Zello and André L. Boehman

The Energy Institute
The Pennsylvania State University
405 Academic Activities Building
University Park, PA 16802

Philip John Young and Francis J. Waller

Air Products and Chemicals, Inc.
Allentown, PA

Introduction

Addition of oxygen to assist the diesel combustion process is by no means a new idea. Significant work has been ongoing for some years regarding oxygenation of diesel fuel through additives and alternative fuels [1,2,3,4]. Oxygen enrichment of intake air has also been considered as a measure to control the PM emission and to improve thermal efficiency. Argonne National Laboratory has developed a membrane that efficiently separates standard air into oxygen and nitrogen. Motivated by this novel method, recent work at University of Wisconsin-Madison has explored the impact of intake composition [5] and compared the impact of fuel oxygenation and intake oxygen enrichment [6]. This recent work shed some light on the effects of intake charge composition, but left many unanswered questions. The work presented here compares oxygenated fuels with oxygen enrichment of intake air. In this case, we are examining the application of Air Products' VSA type A-040/120L Oxygen Generator to improving diesel engine operation.

Experimental

The experimental system consists of an engine test cell (dynamometer, controller), an engine, combustion analysis instrumentation, and emissions analyzers. Figure 1 presents a schematic diagram of the VW TDI 1.9L turbodiesel engine and test cell instrumentation. Steady-state engine operation at 75 % load and 1900 rpm was chosen for this study because oxygenates effect was known as rather pronounced than at low load condition. A pressure transducer, mounted in the glow-plug hole in the first cylinder was used with a shaft encoder to provide time-resolved pressure traces for heat-release rate calculation. Emissions of particulate matter, NO_x, CO, CO_2, HC were measured respectively via BG1 dilution tunnel, FTIR and HFID.

The intake air flow rate was directly measured via an electronic mass air flow sensor. Fuel consumption rate was recorded via fuel tank weight loss using a precision weighing scale and real-time fuel consumption rate was also measured using two separate flowmeters (Micromotion D06) on the fuel flow to the engine and fuel return from the engine. For oxygen enrichment of the intake air, modification to intake air supply line was required. The oxygen was supplied by the oxygen generator (Air Products' VSA type A-040/120L) into the intake air surge tank through a pressure regulator, a metering valve and flowmeter. Fumigation in to the intake surge tank was chosen to allow the thorough mixing of oxygen-air mixture through the subsequent devices such as the air filter, turbocharger and intercooler before entering the intake manifold. With known air flow rates at the desired engine operation condition, the required oxygen flow rate was pre-calculated and was set to obtain the desired volume percent oxygen enrichment. To verify this oxygen enrichment, the oxygen-air mixture was sampled at the air filter by using the Rosemount O_2 analyzer (Model 755R).

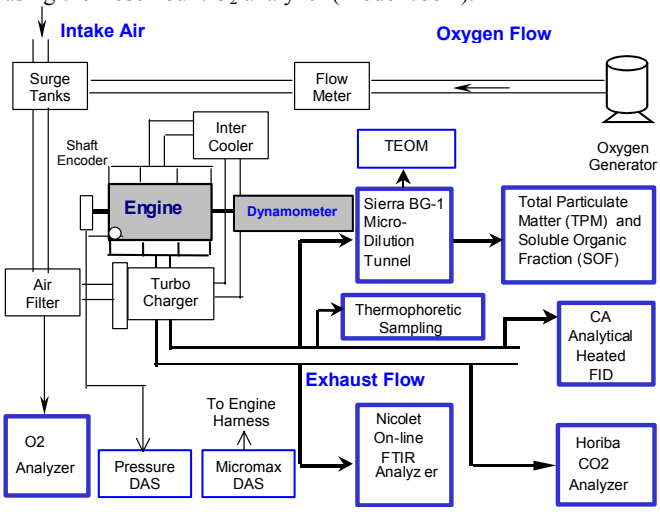

Figure 1. Schematic diagram of the experimental setup

Fuel oxygenation was accomplished using two compounds with widely different cetane number. A mixture of glycol ethers, 20 vol.% monoglyme and 80 vol.% diglyme (referred to as CETANER^{TM}), with a cetane number of 100 represented a cetane-improving oxygenate. In contrast, 1,3-dioxolane with a cetane number of 30 represented a cetane suppressing oxygenate. Both compounds were soluble in diesel fuel and provided a means of identifying the cetane number and oxygen addition effects.

Results and Discussion

The experiments was intended to investigate and compare the relative effect of two oxygen addition methods on emission and combustion, via intake air enrichment and oxygenation of the fuel. To directly compare both intake air oxygen enrichment and oxygenated fuel under the same extent of oxygen addition, oxygen to carbon ratio in the overall mixture was kept constant. An elementary analysis was performed to match the oxygen to carbon ratio on the basis of the overall in-cylinder gas compositions in the same way as Donahue et al. [6].

In Figure 2, oxygen addition, whether it comes from intake air enrichment or via oxygenated fuel, reduces soot even though the extent of PM reduction varies remarkably with oxygen addition method. For the equivalent level of oxygen addition based on oxygen to carbon ratio=5.1, intake air oxygen enrichment was more effective for reducing soot than fuel-bound oxygen addition, such as CETANER^{TM} blends and 1,3-dioxolane blends.

This significant effectiveness of intake air enrichment might be explained by the synergistic effects of the thermal and chemical interaction arising from intake oxygen addition. The heat release rate in Figure 3 indicates that oxygen enrichment lowered the peak premixed burn, which leads to lower soot precursor formation through reduced fuel pyrolysis without any shift in combustion phase from the baseline. The resulting increased heat release in the mixing-controlled combustion phase will also contribute to increased soot oxidization. A similar trend of heat release characteristics has been observed previously for intake air enrichment by Donahue et al. [6].

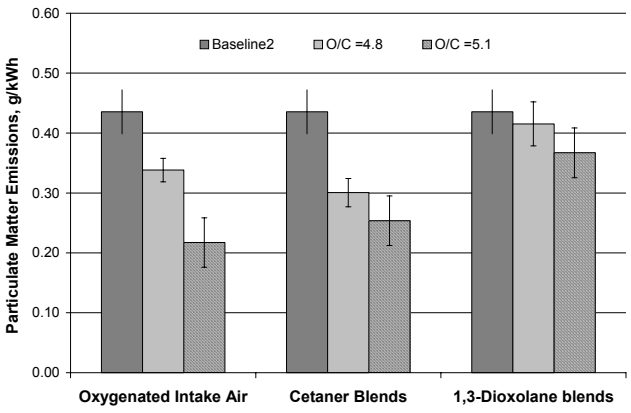

Figure 2. Particulate Matter Emissions for different oxygen addition methods, g/kWh basis.

The other possible explanation is that the presence of OH and O in the mixing-controlled phase will more likely attack the soot precursors, which results in a lower acetylene concentration as postulated by Gülder [7]. The free oxygen supplied by the intake air can be the key species affecting the soot formation chemistry, thereby reducing soot formation and increasing the oxidation of the soot.

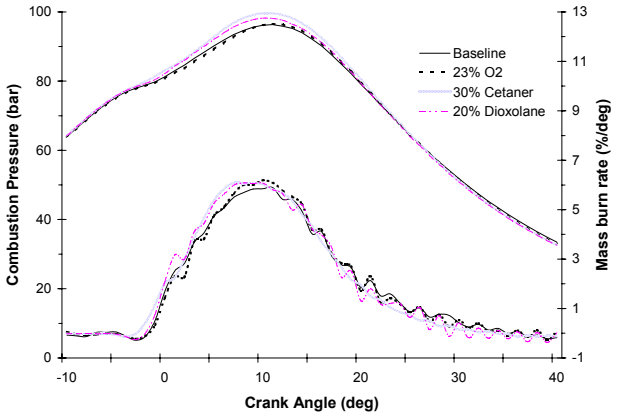

Figure 3. Heat release rate for different oxygen addition methods at O/C=5.1.

The oxygenated fuels were seen to advance the start of injection timing in Figure 3 because the engine maintains power at the requested level through injection timing adjustment to compensate for the higher density and lower heating value of oxygenated fuel as compared to the baseline fuel. Specifically, injection timing of the CETANER^{TM} blend was more advanced than that of 1,3-dioxolane, but the high cetane number of CETANER^{TM} compensates this advanced injection timing so that ignition delay was similar to the baseline and 23% intake air enrichment. Under the same ignition delay, the CETANER^{TM} blend was also observed to lower peak premixed burn as in an intake air enrichment case, which leads to the lower soot formation through reduced fuel pyrolysis. The heat release characteristics of CETANER^{TM} are consistent with the observations reported by Beatrice and coworkers, that premixed burn rate decreases while diffusion heat release rate increases at high load. That high diffusion heat release was attributed to increased oxidation of the combustion intermediates by oxygen present in the additive [8].

The unfavorable effect of oxygen addition on NO_x emissions becomes greater in the order of 1,3-dioxolane, CETANER^{TM} and intake air enrichment as shown in Figure 4. This trend does agree with typical PM-NO_x trade-off behavior, i.e. the lower the PM, the higher the NO_x. In other words, the increased oxygen concentration causes a NO_x increase in all cases, but the extent of the increase depends strongly on how the oxygen is added. Intake air enrichment leads NO_x emissions to increase by 53 and 126 (%) with respect to baseline for 22 (vol.%) and 23 (vol.%) oxygen concentration, respectively. Considering that NO_x is more likely to form in a post flame zone where the mixing controlled regime dominates, heat release in the mixing controlled phase of combustion might be one of the key factors. Under the present engine operation where mixing controlled combustion occurs, the higher heat release rate of the mixing controlled combustion phase leads to higher temperatures for the intake air enrichment case shown in Figure 4. This thermal effect contributes to a NO_x increase in combination with local ϕ (equivalence ratio) effect. According to local ϕ theory, the available oxygen in the high-temperature flame region may shift this locally rich mixture toward a slightly lean mixture where the maximum equilibrium O-atom mole fraction lies [6]. Consequently, the high equilibrium concentration of oxygen atom along with super-equilibrium O-atom results in higher kinetically formed NO_x. The incorporation of the fuel-bonded oxygen mitigates the adverse impact of leaner combustion conditions compared to free oxygen atom from intake air enrichment, causing a smaller NO_x increase compared to oxygen enriched intake air.

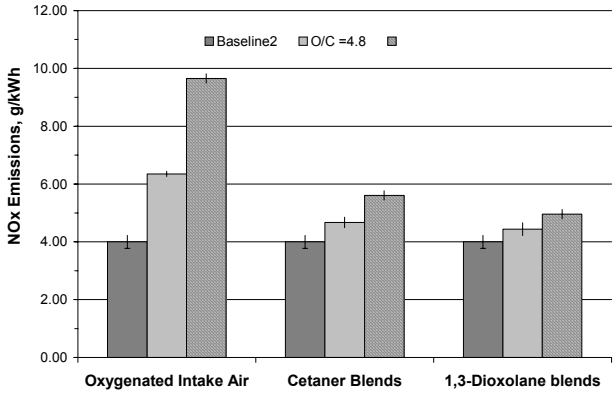

Figure 4. NO_x Emissions for different oxygen addition methods, g/kWh basis

Conclusions

While oxygen enrichment of intake air reduces diesel PM significantly more than fuel oxygenation, fuel oxygenation can provide PM reduction with only a modest affect on NO_x emissions. With their linear structure, the glycol ethers that comprise CETANER^{TM} were shown to be far more effective for soot reduction than equivalent oxygen addition via Dioxolane with its ring structure.

References

(1) Hess et al. In *Chemistry of Diesel Fuels*; Taylor & Francis, **2000**.
(2) Litzinger et al. *IJER*, **2000**, **1**, 57-70.
(3) Hess et al. *SAE*, **2000**, No. 2000-01-2886.
(4) Chapman et al. *SAE*, **2000**, No. 2000-01-2887.
(5) Li et al. *SAE*, **1997**, No. 970322.
(6) Donahue et al. *SAE*, **2000**, No. 2000-01-0512.
(7) Gülder, O.L. *Combustion and Flame*, **1995**, 101, pp.302-310.
(8) Beatrice, C. et al. *SAE*, **1997**, No. 972972.

EARLY SOOT FROM INVERSE DIFFUSION FLAMES

Linda G. Blevins[*]*, Nancy Y.C. Yang*[*]*, George W. Mulholland*[+]*, Ronald W. Davis*[+]*, and Eric B. Steel*[+]

[*]Sandia National Laboratories
Livermore, CA 94550

[+]National Institute of Standards and Technology
Gaithersburg, MD 20899

Introduction

Knowledge of the chemical and physical structure of early soot is useful in the development of soot particle inception models. Dobbins *et al.* established that the earliest soot in a diffusion flame is composed of liquid-like precursor particles laden with polycyclic aromatic hydrocarbons (PAH).[1,2] Electron micrographs of small particle samples from a C_2H_4 diffusion flame centerline indicated an obvious difference between the translucent, liquid-like precursor particles low in the flame and the high-contrast, agglomerated carbonaceous soot high in the flame. We recently used a variety of experimental measurements to demonstrate that the soot exiting a C_2H_4 *inverse* diffusion flame (IDF) is similar in chemical and morphological structure to precursor particles.[3] This finding is significant because IDF exhaust collection allows large samples of young soot to be gathered without invading the flame. Capitalizing on this advantage, a detailed PAH analysis of precursors was provided.[3]

The present paper is an extension of the recent IDF work.[3] It was postulated that IDF soot resembles precursor soot because it exits the flame without experiencing the time/temperature/species conditions leading to carbonization or oxidation.[3] Here, computational results that support this hypothesis are provided. Additionally, while the previous paper analyzed IDF exhaust soot, the current paper addresses soot collected in the IDF tip and its relation to the IDF exhaust soot. Finally, we report the structure of some of the IDF exhaust soot remaining on a quartz filter after the soluble components are extracted with dichloromethane (DCM).

Methods

Experimental. An IDF burner consisting of a 1 cm diameter central air jet surrounded by a 3cm diameter co-annular fuel tube was used. The air flow was 32 mg/s (~35 cm/s) and the C_2H_4 flow was 49 mg/s (~7 cm/s). The visible flame height was 3.5 cm, and an orange cap constituted 90 % of the height. A N_2 flow, necessary to prevent flames between fuel and room air, flowed through an outer annulus. A nearly invisible soot stream exited the IDF. Particles were collected thermophoretically on a 3 mm diameter, 200 mesh copper TEM grid coated with a 20 nm thick carbon substrate in the flame tip (3.5 cm from burner) and in the exhaust (15 cm from burner). The TEM grid was secured to a thin metal spatula and inserted parallel to the flow for three consecutive sub-second intervals. A soot sample on a quartz filter was analyzed using TEM after DCM-soluble components had been removed for a GC/MS analysis provided in our previous paper.[3] The DCM extraction had been performed at 100°C and 13.8 MPa using an accelerated solvent extraction system.[3] The sample was scraped from the filter, dispersed in acetone, and collected onto a lacey grid in preparation for analysis.

Computational. Computations of CH_4 IDFs were performed using direct numerical simulation of the time-dependent Navier Stokes and conserved variable equations for an axisymmetric laminar flame.[4] The simulation employs assumptions of low Mach number, infinite-rate chemical kinetics (flame sheet with a single reaction step), unity Lewis number, variable thermophysical properties, a semi-infinite surrounding fuel-stream, and negligible radiation heat transfer. A CH_4 flame was predicted because these assumptions are more appropriate for CH_4 than for C_2H_4. The air-to-fuel velocity ratio (5:1) was set to the value used in our C_2H_4 laboratory IDFs. Dilute-condition particle tracking incorporating the effects of inertial, thermophoretic, and gravitational forces was included.[5] The computational grid was 3 cm in height.

Results and Discussion

Figure 1 depicts the CH_4 IDF predicted temperature field and the time-temperature history of 40 nm graphite particles introduced at axial positions of 0 mm, 5 mm, 10 mm, 15 mm, and 20 mm from the burner and at radii corresponding to a characteristic soot formation temperature of 1250 K.[6] The figure demonstrates that, after inception, IDF soot moves away from the high temperature region under the influence of thermophoretic forces. This finding supports our previous suggestion that IDF soot does not carbonize or oxidize before exiting the flame.

Figure 2 depicts micrographs of particles collected in the IDF tip. The particles are irregularly shaped. Agglomeration appears absent. The particles are 50 nm -100 nm wide and tall, which is considerably larger than the 20 nm – 30 nm precursor particles of Dobbins *et al.*[1,2] The particles are presumably larger because they are pushed toward the fuel stream into the rich portion of the flame, where they experience a large amount of surface growth but are not fully carbonized or oxidized.[7] The particles have dark centers opaque to the electron beam. They appear to be plate-like structures stacked upon one another, consistent with a recent description of precursor particles.[8] The dark edges around some of the particles suggest the beginning of carbonization.[2,3] The bottom panel of Fig. 2 also shows a small 30 nm particle which appears round or somewhat spherical in the image. It is possible that this is a primary soot particle.

Figure 3 depicts an image of a portion of a large particle collected 15 cm from the burner in the IDF exhaust. The soot appears to be a clump of several of the tip particles shown in Fig. 1. The image shows some spherical primary particles between 30 nm and 60 nm in diameter. Some of the primaries bundle together as if agglomeration is just beginning. Some appear to have coatings and

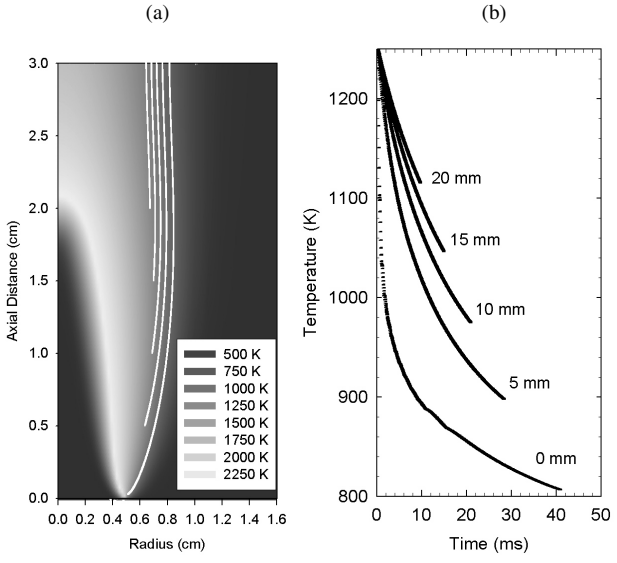

Figure 1. Predicted temperatures and particle time-temperature histories in air/CH_4 IDF. White streaks in (a) are particle pathways. Soot inception is assumed to occur at 1250 K.

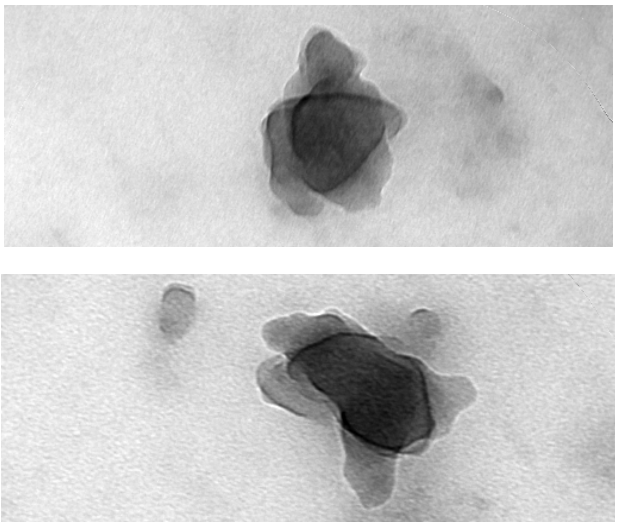

Figure 2 TEMicrographs of particles collected in the orange IDF tip. Each micrograph is 500 nm wide.

material between them, which may indicate that a liquid-like substance is either present or was once present. The carbon in the particles appears amorphous, and the graphitic "onion" structure typical of fully carbonized soot is not visible. Additional exhaust soot micrographs are provided in our previous paper.[3]

Figure 4 depicts a high resolution TEM image of IDF exhaust soot removed from a filter after DCM extraction. Graphite-like onion structures 2 nm to 5 nm in size appear. The frequency of occurrence of the onions in the IDF soot is not known, although it is possible that they are ~40% of particle mass based on our previous organic/graphitic fraction measurements.[3] The onions do not appear in the non-extracted soot of Fig. 3. They may be disguised by heavy PAH or precursor material coating (~50% was DCM-soluble[3]). The existence of turbostratic structures are thought to indicate that carbonization or tempering has occurred.[8,9] If so, the soot left on the filter is partially carbonized, consistent with the higher C/H ratio of IDF soot (~2.5)[3] relative to precursors (~1.8).[1] The onions may

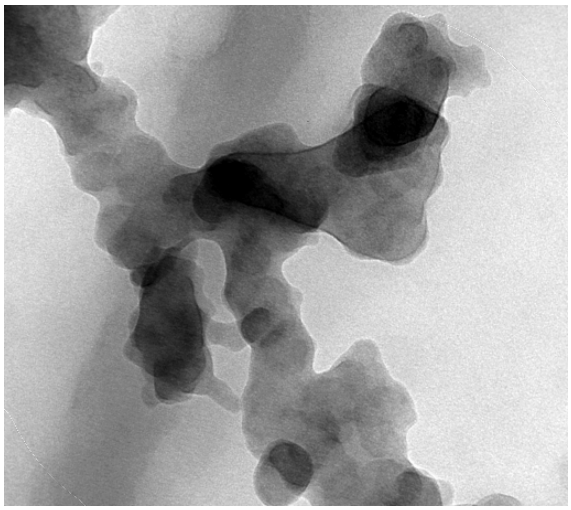

Figure 3 TEMicrograph of a complex particle collected from the C_2H_4 IDF exhaust stream. The image is 500 nm wide. The background line is an artifact of the grid carbon film substrate.

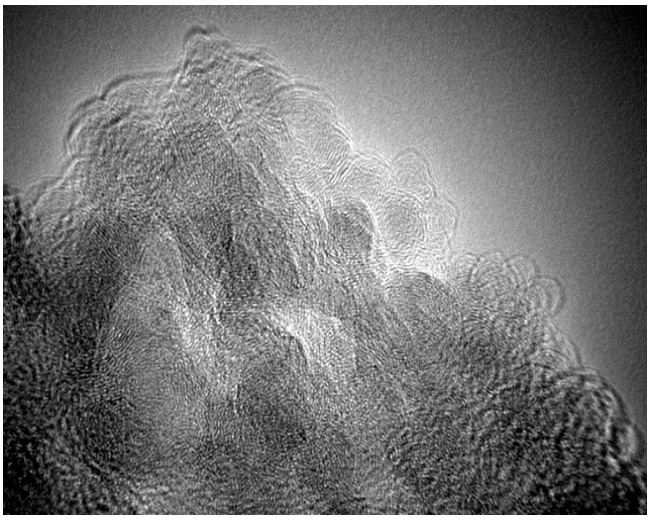

Figure 4 High-resolution TEMicrograph of IDF exhaust soot after DCM extraction. The micrograph is 78 nm wide.

occur because a portion of the soot is swept inward near the tip by buoyancy. They may also be an artifact of extraction. However, Chen and Dobbins provide evidence of the beginnings of crystal structure in precursor particles from normal diffusion flames.[8] There is a possibility that the structures may be associated with the precursors themselves. This prospect warrants further investigation.

Conclusions

Numerical predictions of particle pathways verify that IDF soot particles cool after they are formed and do not experience time-temperature paths associated with carbonization. Soot particles collected in an IDF tip are large, stacked, plate-like particles. By the time they reach the exhaust, the particles have clumped together and appear to be surrounded by liquid-like material. Beneath the liquid-like material, at least a few ordered soot structures are present. The results are providing insight into soot inception and growth in diffusion flames.

Acknowledgements. Support from Strategic Environmental Research and Development Program (Charles Pellerin) and National Aeronautics and Space Administration (Peter Sunderland) is acknowledged. Sandia is a multi-program laboratory operated by Sandia Corporation, a Lockheed Martin Company, for the United States Department of Energy under contract DE-AC04-94-AL85000.

References

(1) Dobbins, R. A.; Fletcher, R. A.; Chang, H. C. *Combust. Flame* **1998**, *115*(3), 285.
(2) Dobbins, R. A. *Physical and Chemical Aspects of Combustion: A Tribute to Irvin Glassman*; Dryer, F. L.; Sawyer, R. F., Editors; Gordon and Breach: Newark, NJ, 1997; pp 107-133.
(3) Blevins, L. G.; Fletcher, R. A.; Benner, B. A.; Steel, E. B.; Mulholland, G. W. *Submitted to Proceedings of the Combustion Institute* **2002**, *29*.
(4) Davis, R. W.; Moore, E. F.; Santoro, R. J.; Ness, J. R. *Combust. Sci. Technol.* **1990**, *73*(4-6), 625.
(5) Davis, R. W.; Moore, E. F.; Zachariah, M. R. *J. Cryst. Growth* **1993**, *132*(3-4), 513.
(6) Du, J.; Axelbaum, R. L. *Combust. Flame* **1995**, *100*(3), 367.
(7) Kaplan, C. R.; Kailasanath, K. *Combust. Flame* **2001**, *124*(1-2), 275.
(8) Chen, H. X.; Dobbins, R. A. *Combust. Sci. Technol.* **2000**, *159* 109.
(9) Grieco, W. J.; Howard, J. B.; Rainey, L. C.; Vandersande, J. B. *Carbon* **2000**, *38*(4), 597.

FULLY-INTEGRATED MOLECULAR DYNAMICS – KINETIC MONTE CARLO CODE: A NEW TOOL FOR THE STUDY OF SOOT PRECURSOR GROWTH IN COMBUSTION CONDITIONS

A.Violi[1], A. Kubota[2], W. Pitz[2], C. K. Westbrook[2], A. F. Sarofim[1]

[1]Department of Chemical & Fuels Engineering
University of Utah, Salt Sake City, Utah 84112 - USA
[2]Lawrence Livermore National Laboratories, Chemistry and Materials Science Directorate, Livermore, CA 94551- USA

Introduction

Formation of soot and other carbonaceous material during the incomplete combustion of hydrocarbons is one of the least resolved problems; despite essential progress in understanding single processes, the comprehensive theory and models that predict the formation of these compounds fall short of predicting many of the experimental observations.

The transformation from low molecular weight organic gas phase species to particulate matter is not well understood since high molecular weight carbonaceous species formed during this process are difficult to analyze with certainty by conventional methods. Recent advances in experimental and modeling investigations in combustion have shown that a much larger amount of carbonaceous material, besides soot and GC-identifiable PAHs, is emitted in form of organic carbon (tar-like material) than were thought some years ago.[1-2] Following recent experimental characterization of this material,[1-2345-6], we developed a kinetic mechanism in which high molecular mass aromatic compounds are postulated to form by the reactive polymerization of small PAH [7-9]. The mechanism involves a sequence of chemical reactions between aromatic compounds with 6 π-electron, i.e. benzene, naphthalene, and cyclo-penta fused compounds i.e., acenaphthylene, indene. The distinguishing features of this mechanism and its importance in explaining experimental observations is reported elsewhere,[8] together with a detailed quantum mechanic analysis of the first steps of the reaction sequence.

The work presented here adds one step more to the study of this process. The aim of this paper is to introduce a new tool for examining the molecular transformations from gas phase precursors to soot-like material. This new approach combines two common methods: Kinetic Monte Carlo (KMC) and Molecular Dynamics (MD). In the new code, KMC and MD are fully integrated in such a way that any reaction process for the KMC time step is much larger than the time required for relaxation during MD. The kinetic rates are calculated using high-level quantum chemical methods. The code is employed to study a low-pressure laminar premixed benzene/oxygen/argon flame and some preliminary results are reported for the H/C ratio of soot precursors. The use of this new code can provide at the long term potential for information on soot precursor characteristics.

Computational details

The Fully-Integrated KMC/MD code combines the strengths of two common simulation methods: Kinetic Monte Carlo (KMC)[10] and Molecular Dynamics (MD)[11]. This approach allows sampling long time-scales, where the time-duration between Monte Carlo events can be arbitrarily long (depending on the kinetics, model. etc), while in molecular dynamics, we require time steps which are a small fraction of the atomic vibrational period. So the combination of the two techniques spans two time- and equilibrium scales, MD allows for relaxation as well as processes very far from equilibrium, while the KMC part allows much larger time-scale changes to the system, provided that the system is at equilibrium.

Structure simulation

The sequence of steps repeated in the Fully-Integrated KMC/MD code are reported in Figure 1.

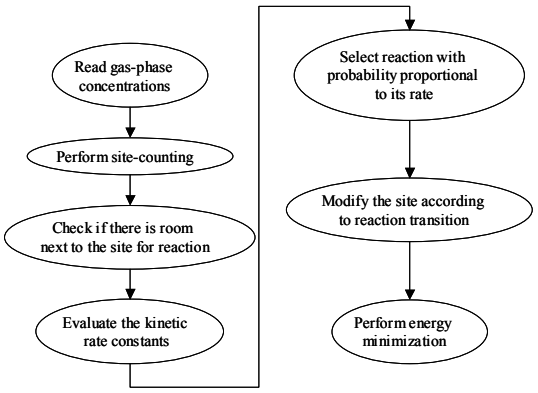

Figure 1. Sequence of steps repeated in the KMC/MD code

The code first reads the gas-phase concentrations (typically from the user or another application), then performs a site-counting procedure to identify every atom with a local environment which fits the definition of each site, including proximity conditions. The sites included into the code are described elsewhere[12].

As a next step the code evaluates the kinetic rate constants on a per-site basis as well as the reaction rates. Kinetic parameters for the possible reactions among the species present in the systems have been evaluated using the Transition State Theory (TST),[13] and the Evan–Polanyi linear free-energy formula[14] within the reaction class TST formalism, to provide activation energies of reactions in a given reaction class. The potential energy information were calculated using the hybrid density functional B3LYP method[15] (i.e. B3LYP/6-31G(d,p).[16]).

The Evan–Polanyi linear free-energy formula was used to derive the activation energies in a given reaction class, such as H-abstraction reaction rates were calculated.[17].

After this step, the code selects a reaction with probability proportional to its rate, and then perform modification of the site according to the reaction transition. Reaction sites have been defined in the context of the empirical bond-order potentials of Brenner,[18] which is able to capture many of the essential features of chemical bonding in hydrocarbons. The analytical function is a highly parametrized version of Tersoff's empirical-bond-order formalism[19].

The last step is represented by the molecular dynamics calculation and it consists in the energy minimization of the newly obtained structure. High molecular mass compound growth is here modeled in the environment of a low-pressure laminar premixed benzene / oxygen / argon flame[20].

Results and Discussion

Starting from a gas-phase bulk containing acenaphthylene, naphthalene and H, the calculations follow the growth of an individual substrate (in this case naphthalene) to which compounds from the bulk are added..

In order to show the importance of Molecular Dynamics module in this method, we analyze the structure reported in Fig.2.

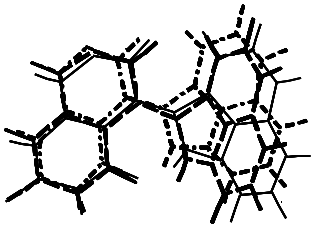

Figure 2. Structural modification during relaxation.

The compound $C_{22}H_{13}$ represents an intermediate produced during the molecular growth process. The figure shows the changes that occur to the structure after a relaxation of few ps using the molecular dynamics module, which allows the structure to reach a relaxed local minimum. The dashed line shows the change that occur after 1 ps, and the solid line reports the structure after 2 ps. The importance of this module is straightforward. The calculations lead insight into proximity conditions and site dependencies for cyclodehydrogenation reactions.

After the application of the Molecular Dynamics, new reactions and reaction sites are identified, and the Kinetic Monte Carlo module is applied for a given interval to calculate the new structures formed. Examples of structural evolutions of high molecular mass compounds are shown in Fig. 3 for the system selected (starting compound is naphthalene). Structure 2 ($C_{64}H_{38}$) is formed from Structure 1 through H abstraction and further addition of 2 molecules of naphthalene and 1 acenaphthalene. After further H abstraction and naphthalene addition, Structure 3 ($C_{94}H_{50}$) is produced.

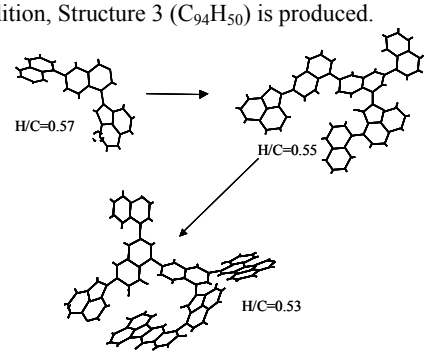

Figure 3. Structural evolution of aromatics

The introduction of ring closure reactions by dehydrogenation in the kinetic scheme allows the formation of curved structures. The H/C ratio of the structures slowly decreases going from 0.57 for the first structure to 0.53 for the last in the present limited simulation.

Evidences for molecules such as shown in Fig.3 is provided by Homann and co-workers,[21] who analyzed large PAH molecules and radicals in a similar benzene flame.

The combination of the polymerization mechanism together with KMC/MD code allow us to build compounds with H/C ratios in the range identified by the authors. This would not be possible with a mechanism that allows only the formation of fused aromatic. More than that this approach can provide information on the chemical structure of the compounds during their growth.

Further work such as a larger number of simulations can give statistical information about the system, i.e. H/C and molecular weight distribution, and morphology as a function of the time.

Conclusions

This paper is directed at the development of a new tool for examining the molecular transformations from gas phase precursors to soot. A new code, named Fully-Integrated KMC/MD, has been developed and employed to analyze possible growth pathways that lead to high molecular mass compounds. This code puts the two simulation procedures (KMC and MD) on an equal footing and involves alternating between MD and MC steps during the simulation. The code was used to analyze some experimental results obtained by Prof. Homann's research group. The environment chosen for this analysis is a low-pressure laminar premixed benzene/oxygen/argon flame. The open structures obtained with the reaction scheme presented above and the code provide an explanation for the H/C ratios of soot precursors and young soots being greatly higher than those of polybenzenoid structures of equal molecular weight. Also, the curvature introduced by forming five- and six-membered rings is the most noticeable feature of these structures.

The knowledge of the structures of soot precursor compounds is important to further progress with respect to the question about soot formation models by applying the KMC/MD code to follow the time-evolution of a statistical ensemble of molecules, as well as the time-evolution of extremely large molecules.

Acknowledgment. This research is funded by the University of Utah Center for the Simulation of Accidental Fires and Explosions (C-SAFE), funded by the Department of Energy, Lawrence Livermore National Laboratory, under subcontract B341493. This work was performed under the auspices of the U.S. Department of Energy by University of California Lawrence Livermore National Laboratory under contract number W-7405-Eng-48

References

1.Ciajolo, A., D'Anna, A., Barbella, R., Tregrossi, A., *Proc. Combust. Inst*. 25: 1994, p. 679.
2.Lam, F. W., Longwell, J. P., Howard, J. B., *Proc. Combust. Inst*. 23: 1990, p. 1477.
3.Ciajolo, A., D'Anna, A., Barbella, R., Tregrossi, A., Violi, A., *Proc. Combust. Inst.* 26: 1996, p. 2327.
4.Bachmann, M., Wiese, W., Homann, K-H., *Proc. Combust. Inst*. 26: 1996, p. 2259.
5.D'Alessio, A., D'Anna, A., D'Orsi, A., Minutolo, P., Barbella, R., Ciajolo A., *Proc. Combust. Inst*. 24: 1992, p. 973.
6.Minutolo, P., Gambi, G., D'Alessio, A., *Proc. Combust. Inst.* 27: 1998, p. 1461.
7 D'Anna, A., Violi, A., D'Alessio, A., Combust. Flame 121:418-429 (2000)
8 Violi A., Truong T.N., Sarofim A.F., Combust. Flame 126: 1506 (2001)
9 D'Anna A., Violi A., D'Alessio A., Sarofim A.F., Combust. Flame 127:1995 (2001)
10 Alder B.J., Wainwright T.E., J. Chem. Phys 31: 459 (1959)
11 Haile, J.M., Molecular Dynamics Simulation: Elementary Methods, John Wiley & Sons, New York, (1992)
[12] Violi A., Kubota, A., Truong T.N., Pitz W., Westbrook C.K., Sarofim A.F., submitted to the XXIX Symposium on Combustion, August 2002.
13 http://vklab.hec.utah.edu
14 Zhang, S. and Truong, T.N. J. Phys. Chem. A. In preparation
15 Frisch, M. J., et al., Gaussian 98, Revision A.7, Gaussian, Inc., Pittsburgh PA, 1998
16 Hehre, W., Radom, L., Schleyer, P., R., Pople, J. A., Ab initio Molecular Orbital Theory, Wiley, New York, 1986
17 Violi, A., Sarofim, A.F., Truong, T.N., Proc. To The 2nd International Mediterranean Combustion Symposium, Egypt, January 6-13 2002, in press
18 Brenner, D.W., Physical Review B 42: 9458 (1990)
19 Tersoff, J., Physical Review Letters 61: 2879 (1988)
20 Bittner, J.D., Howard, J.B., Particulate Carbon: Formation during Combustion, Siegla D.C. and Smith G.W., Ed., Plenum Press, New York, 1981, p.109
21 Keller, A., Kovacs, R., Homann, K.-H., Phys. Chem. Chem. Phys. 2:1667 (2000)

MODEL COMPOUND STUDY OF THE PATHWAYS FOR AROMATIC HYDROCARBON FORMATION IN SOOT

Nancy A. Tomczyk[1], Jerry E. Hunt[1], Randall E. Winans[1], Mark S. Solum[2], Ronald J. Pugmire[2], and Thomas H. Fletcher[3]

[1]Chemistry Division, Argonne National Laboratory, Argonne, IL 60439, navan@anl.gov; [2]Dept. of Chemical and Fuels Engineering, University of Utah, Salt Lake City, UT 84112; [3]Dept. of Chemical Engineering, Brigham Young University, Provo, UT 84602.

Introduction

To explore the mechanisms for formation of aromatic hydrocarbons as precursors to soot, a model system using combustion of biphenyl in a fuel rich flame is studied. The soots acquired at three different temperatures are solvent extracted and the extract characterized by both GCMS and high resolution mass spectrometry. A description of the NMR results for the whole soots has been published (1). The production of most products could be rationalized from the coupling of biphenyls and subsequent aromatic species and the addition of acetylenes to existing aromatic molecules. Early work by Badger on pyrolysis of hydrocarbons is used in developing these schemes (2). The reaction schemes to produce larger aromatic hydrocarbons will be discussed. Richter and Howard have discussed in detail potential reaction mechanisms in the formation of aromatics as precursors to soot (3).

Experimental

Soot samples from biphenyl are collected at three temperatures. Details on the samples are given in reference 1. The samples are extracted at room temperature with methylene chloride. Desorption electron impact high resolution mass spectra (DEIHRMS) are taken on a 3-sector MS-50 (4). Samples are heated on a probe from 200 to 700 °C at 200 °C/min. directly in the source. Precise mass measurements are averaged from scans over the entire temperature range. Formulae are assigned and the data sorted via a procedure developed in house. High resolution mass spectrometry data is sorted by both heteroatom content and by hydrogen deficiency, which is also termed double-bond equivalents (dbe). From hydrogen deficiency, the size of aromatic clusters can be estimated. GCMS data are obtained using a Hewlett Packard 6890 gas chromatograph with a 5973 quadrupole mass selective detector. The injection system is a CDS pyrolysis injector. The samples are placed in a quartz tube and the solvent is allowed to evaporate prior to analysis. The sample is pyrolyzed at 600ºC while a stream of helium passed over the sample and onto the column. The column used is a 60 meter J&W DB-17HT with a 0.25 mm id and a film thickness of 0.25 µm. The oven is held at 40ºC for 1 minute, then ramped at 6ºC/minute to 280 ºC. It is held there for 10 minutes. The quadrupole is held at 150 ºC, and the source is at 230 ºC.

Results

The structure and formation of the most abundant aromatic hydrocarbons (relative abundance >10) will be discussed. All of these species can be rationalized from the pyrolysis of biphenyl (1). Growth to larger molecules occurs by dimerization of aromatics and by acetylene addition. Both of these growth mechanisms have been suggested for soot formation. Analysis of these data suggest that both pathways are occurring along with a small amount of methylation and insertion of methylenes. The structures are deduced from the precursors and from molecular formulae. In some cases, especially in C_2 addition, multiple isomers probably exist and a representation is shown. Only in the lowest temperature sample is biphenylene observed and is formed from the loss of two hydrogens. Biphenylene has been prepared in a high temperature plasma for biphenyl.

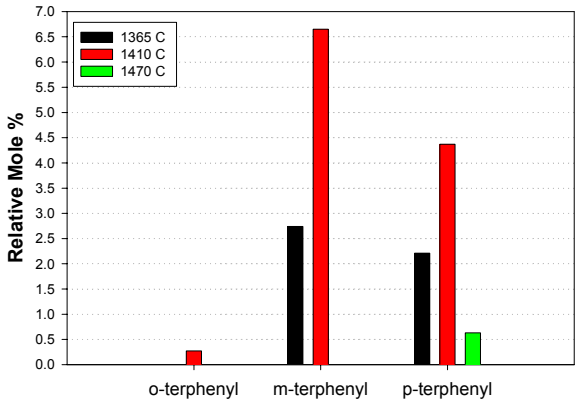

Figure 1. Distribution of terphenyl molecules from GCMS

All three isomers of terphenyl are observed in both GCMS (the data for the three temperatures are shown in Figure 1) and HRMS and result from the coupling of biphenyl with a benzene radical. Benzene radicals will form readily from cleavage of biphenyl. O-terphenyl [1] can be transformed simply by a loss of H_2 to form triphenylene [2]. This terphenyl is found in the least amount of all three possible isomers in the 1410 K sample (Figure 1), which can be explained by its loss to triphenylene. The addition of acetylene (C_2) gives a benz[e]pyrene [3]. The addition of one more C_2 results in benzo[ghi]perylene [4] and the next addition of C_2 yields coronene [5]. In each of these cases only one isomer is possible and [1]-[4] have been identified by GCMS and the formulae for all five observed in HRMS.

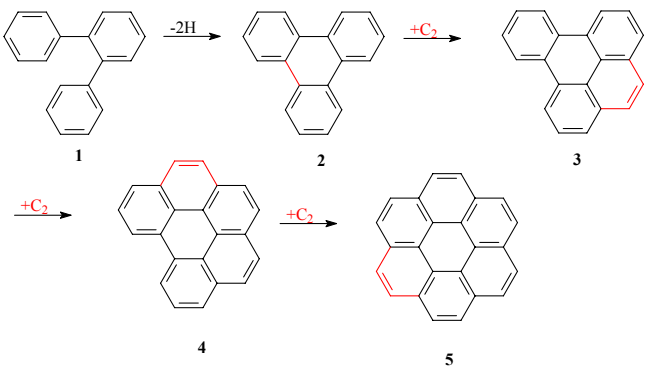

The m-terphenyl[6] gives a much different suite of products and does not yield molecules in the pyrene family. The addition of C_2 gives a phenyl-phenanthrene [7] and with the addition of a second C_2 is transformed into dibenz[a,j]anthracene [8]. This molecule [8] has been observed in soots in a number of studies (5). At the lower temperature (1365) two hydrogenated products, the 1,2-dihydro [9] and the 7,14-dihydro [10], are observed in the MS. These hydroaromatics appear not to survive at the higher temperatures.

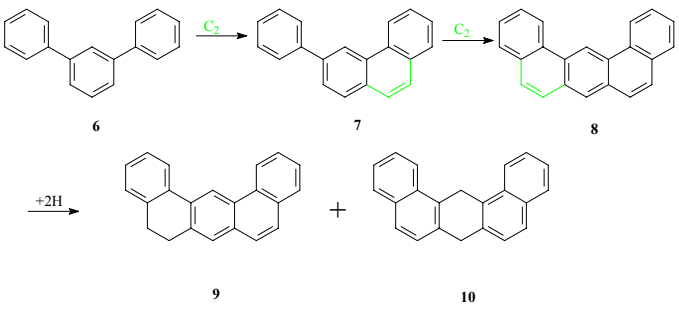

There are non-direct pathways to molecules such as perylene [11]. Under pyrolysis conditions the loss of C_2 from phenanthrene to form biphenyl has been observed(6). Direct pathways from biphenyl to [11] are no readily apparent.

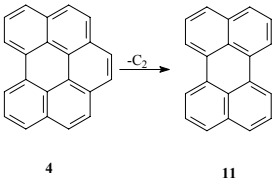

Larger PAHs are observed in the HRMS data, but structures can only be deduced from the smaller products characterized by GCMS and logical pathways that have been elucidated for their formation. For example, $C_{32}H_{16}$ which is found at the two higher temperatures could result from the dimerization of pyrene or the combination of pyrene with phenanthrene with the addition of C_2.

Conclusions

This approach simplifies what is typically a very complex process in the formation of soot in flames. Reaction schemes can be developed which can be rationalized by the relatively simple product mix. Both aromatic coupling and the addition of acetylene appear to be important.

Acknowledgment. This work was performed under the auspices of the Office of Basic Energy Sciences, Division of Chemical Sciences, Geosciences, and Biosciences, U.S. Department of Energy, under contract number W-31-109-ENG-38.

References

(1) Solum, M. S.; Sarofim, A. F.; Pugmire, R. J.; Fletcher, T. H.; Zhang, H. *Energy Fuels*, **2001**, *15*, 961-971.
(2) Badger, G. M. *Progr. Phys. Org. Chem.,* **1965**, *3*, 1-40.
(3) Richter, H.; Howard, J. B. *Progress in Energy and Combustion Science,* **2000**, 26, 565–608.
(4) Winans, R.E. In *Advances in Coal Spectroscopy*, H. L. C. Meuzelaar, Ed., Plenum Press: New York, 1992, pp. 141-164.
(5) Wornat, Mary J.; Ledesma, Elmer B.; Sandrowitz, Alyssa K.; Roth, Mark J.; Dawsey, Sanford M.; Qiao, You-Lin; Chen, Wen *Environmental Science and Technology* **2001**, *35*, 1943-1952.
(6) Krabiell, K.; Wanzl, W.; Juentgen, H. Coal Sci. Technol. **1987**, *11*(Int. Conf. Coal Sci., 1987), 687-90.

OBSERVATION AND COLLECTION OF AN AEROSOL IN ETHANE AT 1184 K

Greg F. Glasier and Philip D. Pacey

Department of Chemistry, Dalhousie University, Halifax, Nova Scotia, Canada, B3H 4J3

Introduction

Soot is formed in the pyrolysis regions of flames. Study of soot formation is made difficult by the sharp temperature and concentration gradients existing in flames. Carbon is also formed in the pyrolysis of fuels in the absence of oxygen. Here the gradients are more gradual, but the chemical process is still not completely understood. Accordingly, a multi-facetted study has been undertaken of the formation of carbon during the pyrolysis of ethane at 1184 K. The conditions employed were close to those used in industrial steam cracking.

Experimental

A vertical, cylindrical, quartz reactor (1.0 cm i.d.) was heated by a 48-cm long, resistive furnace. Ethane (Matheson, 99.95% pure) entered the reactor at the top or bottom at a rate controlled by an MKS 1159B controller. The pressure of gas in the reactor was controlled using an MKS 122A pressure transducer, an Omega CN-2000 controller and an MKS 159A solenoid valve.

Gaseous products were analysed by gas chromatography. Condensible products were trapped cryogenically and were analysed by liquid chromatography, gas chromatography and mass spectrometry. Formation of solid carbon on a cylindrical substrate (3 mm o.d., 50 mm long), suspended in the hot zone, was monitored using an electronic microbalance (Cahn RG2000).

In some experiments ethane entered the reactor at the bottom and an equal volume of argon entered the top, with both gases exitting through a T-joint at the mid-point of the hot zone. Light from a diode laser (Alpec, 670 nm) was directed along the axis of the reactor and onto a photodiode at the opposite end. Either a gold wire grid (Electron Microscopy Sciences, 200-Au50) or a quartz disk (7 mm o.d., 3 mm thick) was suspended and heated in the upper, argon-blanketed part of the reactor and was dropped through the hydrocarbons in the lower part of the reactor. The wire grids were removed from the system and examined by transmission electron microscopy (TEM, Philips, EM201). The quartz disks were coated with gold (Sam-Sputter-2A) and examined by scanning electron microscopy (SEM, Bausch and Lomb, Nanolab 2000). Fluorescence spectra were recorded with a Shimadzu spectrofluorophotometer (RF-5301 PC). SEM images were interpreted with the aid of Scion image analysis software.

Results and Discussion

The major gaseous products were ethylene, methane and hydrogen. At residence times of a few seconds, the yield of condensible products increased until they accounted for 30% of the mass of ethane fed. The rate of formation of condensible products correlated strongly with the concentration of acetylene in the reacting mixture. The rate of formation of carbon did not correlate with the concentration of acetylene, but was strongly correlated with the concentration of condensible products. These observations were consistent with acetylene acting as a precursor to the formation of condensible products, which, in turn, acted as precursors to the formation of carbon.

Analysis of the condensible products revealed the presence of benzene, styrene and a number of polynuclear aromatic hydrocarbons (PAHs). The simpler species, such as naphthalene, acenaphthalene, anthracene, phenanthrene and pyrene were quantified. A number of other PAHs were identified. The molecular masses of the products extended up to 700 amu. Species with even numbers of carbon atoms dominated. The distribution of PAHs resembled those that have been observed in flames.

When the reactor was examined by eye, its contents appeared to glow with an orange light. The transmitted intensity of the diode laser radiation was attenuated by an amount that increased with increasing residence time of the gases in the reactor. The laser attenuation nicely paralleled both the yield of condensible products and the rate of carbon deposition. These observations were consistent with the presence of an aerosol. The aerosol could have been formed from the liquid products or in parallel with the liquid products. The aerosol, like the liquid products, was a potential source of carbon in the system.

The wire grids, which had been dropped through the aerosol, were found by TEM to have collected tiny hemispheres from the aerosol. The hemispheres ranged in diameter from 4 to 260 nm. Their shapes were consistent with the presence of a population of spherical, liquid droplets, which partially flattened on striking the wires. Some of the hemispheres had smaller circles on their surfaces, suggesting that they may have been formed by coagulation of smaller droplets.

The hemispheres were found to be soluble in dichloromethane. The resulting solution had fluorescence maxima at 380, 415 and 440 nm, where emission would be expected from three- and four-ring PAH units. Unsubstituted four-ring PAHs are too volatile to condense at 1184 K, but such PAH units could have been linked to other PAH units to form nonvolatile compounds.

The SEM images revealed the presence of tiny circles on the surfaces of the quartz disks. The circles ranged in diameter from 10 to 240 nm. Square sections of the surface were scanned and the circles were measured and counted. The diameters of the observed hemispheres were converted to those of spheres of the same volume.

The greatest number of particles were found in the center of the bottom face of the quartz disk. This corresponded to a stagnation point, where the gases flowing past the falling disk would separate to move over the face of the disk. Here the average diameter of the gas-borne spheres was calculated to be 52 nm. The hemispheres were less numerous near the outer edge of the face and on the sides of the disk. Here the average diameters were 46 and 34 nm, respectively.

Assuming the density of the hemispheres was equal to that of coronene, the rate of deposition of material on the side of the disk was found to be similar to the rate of deposition of carbon on the cylindrical, quartz substrate, as previously measured with the microbalance. This was consistent with deposition of the droplets, followed by their carbonization on the surface.

The gap between the falling disk and the reactor wall had the form of an annulus. Through this annulus all the gases and aerosol particles had to pass, while the disk was falling to the bottom of the reactor. During this passage, a certain fraction of the droplets would reach the side of the disk by Brownian diffusion and would stick there. Fan et al. have considered diffusion of small particles to the surface of an annulus. Using their solution and the observed distribution of droplets on the side of the disk, it was possible to calculate the distribution of droplet sizes suspended in the gas phase. The median diameter was 36 nm and the average diameter

was 42 nm. The distribution followed a log normal function and had a geometric standard deviation of 1.6.

The droplets observed here are somewhat larger than the incipient soot particles that have been observed in combustion. For example, Bonne et al. observed that the most probable particle size increased from 9 to 17 nm with increasing height above the burner. Wersborg et al. found the average diameter increased from 4 to 22 nm with increasing height. In previous pyrolytic studies, Graham et al. used laser scattering to determine mean particle diameters between 12 and 36 nm.

Conclusions

A pyrolytic aerosol has been observed, collected and partially characterized. The aerosol appeared to consist of spherical droplets, which had a log normal size distribution, with an average diameter of 42 nm. The droplets were soluble in dichloromethane and fluoresced at 380 to 440 nm. They were similar to, but larger than, incipient soot particles.

The time dependence of the scattering by the aerosol was consistent with the following mechanism: Acetylene was formed from ethane and ethylene by radical reactions, and went on to form aromatics. Heavy aromatic compounds could condense to form the aerosol observed. This aerosol and the remaining, gaseous aromatic compounds could deposit on surfaces, where they could dehydrogenate to form carbon.

Acknowledgement. The authors wish to thank Imperial Oil Ltd for a University Research Grant, R. Filfil, S. Fry and P. Li for experimental assistance, C. Cawood for a literature survey and D. Slim for valuable discussions.

References

(1) Homann, K.-H. *Angew.Chem.Int. Ed.*, **1998***, 37*, 2434.
(2) Chan, K.Y.G.; Inal, F.; Senkan, S. *Ind. Eng.Chem. Res.* **1998**, *37*, 901.
(3) Scion Image 3b, Scion Corporation, Frederick, MD, 1999.
(4) LaFleur, A.L.; Taghizadeh, K.; Howard, J.B.; Anacleto, J.F.; Quilliam, M.A. *J. Amer. Soc. Mass Spectrom.* **1996,** *7,* 276.
(5) Acree, W.E.; Tucker, S.A.; Fetzer, J.C. *Polycyclic Aromat. Compd.* **1991,** *2,* 75.
(6) Fan, B.J.; Cheng, Y.S.; Yeh, H.C. *Aerosol Sci. Technol.* **1996,** *25,* 113.
(7) Bonne, U.; Homann, K.-H.; Wagner, H.G. *Symp. (Int.) Combust., [Proc.], 10th,* **1965,** 503.
(8) Wersborg, B.L.; Howard, J.B.; Williams, G.C. *Symp. (Int.) Combust., [Proc.], 14th,* **1973,** 929.
(9) Wersborg, B.L.; Fox, L.K.; Howard, J.B. *Combust. Flame* **1975,** *24,* 1.
(10) Graham, S.C.; Homer, J.B.; Rosenfeld, J.L.J. *Proc. R. Soc. Lond. A,* **1975,** *344,* 259.
(11) Graham, S.C. *Symp. (Int.) Combust., [Proc.], 16th,* **1977,** 663.

ON THE FORMATION OF THE FIRST AROMATIC RING

N. W. Moriarty,[a] X. Krokidis,[b] W. A. Lester, Jr.,[c,d] and M. Frenklach[e,f]

[a]Division of Physical Biosciences, Lawrence Berkeley National Laboratory, Berkeley, CA 94720, USA.
[b]Accelrys, Inc., Parc Club Orsay Universit´e, 20 rue Jean Rostand, 91898 Orsay Cedex, France.
[c]Department of Chemistry, University of California at Berkeley, Berkeley, CA 94720-1640, USA.
[d]Chemical Sciences Division, Lawrence Berkeley National Laboratory, Berkeley, CA 94720, USA.
[e]Department of Mechanical Engineering, University of California at Berkeley, Berkeley, CA 94720-1740, USA.
[f]Environmental Energy Technologies Division, Lawrence Berkeley National Laboratory, Berkeley, CA 94720, USA.

Introduction

Formation and growth of aromatic species bridges the main combustion zone chemistry with soot formation. In addition, aromatic molecules are themselves toxic and subject to environmental regulations. The chemistry of aromatics at combustion temperatures is only recently received detailed attention. The primary focus is the formation of the first aromatic ring from small aliphatics, because this step is perceived by many to be the rate-limiting step in the reaction sequence to larger aromatics. Arguments revolve among several possibilities. Here we review some of our recent results obtained using Quantum Monte Carlo calculations.

Theoretical Approach

The quantum Monte Carlo method in the diffusion Monte Carlo (DMC) variant[1] was used for single point calculations at the critical points of the reaction pathway. The independent-particle portion of the trial function was a single determinant of natural orbitals obtained from a Multi-Configuration Self-Consistent Field (MCSCF) calculation that used the Stevens-Basch-Krauss effective core potentials and the following basis sets for hydrogen, (21s1p1d/3s1p1d) and carbon, (16s16p1d1f/3s3p1d1f).[2]

Geometry optimizations were performed at all stationary points on the potential energy surface (PES). A number of Density Functional Theory (DFT) methods was used including the Becke3 and Lee-Yang-Parr (B3-LYP) functional. Geometry optimization was performed with all methods using the standard 6-31G(d,p) basis set. The optimized B3-LYP/6-31G(d,p) geometries were used for the QMC trial wavefunction calculations.

The convergence of the geometry optimization was determined by performing a small number of optimizations for a number of the stationary points on the PES using the valence quadruple zeta cc-pVQZ basis set. All stationary point geometries were characterized by a frequency calculation to confirm their status as minima (no imaginary frequencies) or transition states (one imaginary frequency).

The species heats of formation were calculated at the previously mentioned levels. In addition, some model chemistry methods were explored. One specifically designed for the calculation of radicals is CBS-RAD which uses the Complete Basis Set technique. G2 and the more recent G3 (all of which include MP2 optimization steps) were also included.

The chemically-activated reaction pathways were examined employing recently updated Multi-Well code of Barker.[3] The reaction barriers and conventionally scaled frequencies were used along with moments of inertia determined at the optimized geometries. Lennard-Jones parameters were taken from empirically determined formulae. The real frequencies below 150 cm^{-1} were examined by graphically visualizing the associated normal mode vibrations to identify internal rotational modes that were subsequently treated as free rotors. Simulations were performed for a range of temperatures and pressures and were run to chemical equilibrium.

Even-Carbon-Atom Pathways

Among these are the even-carbon-atom pathways that involve the addition of acetylene to n-C_4H_3 and n-C_4H_5,

$$n\text{-}C_4H_3 + C_2H_2 \rightarrow \text{phenyl} \quad (1)$$

$$n\text{-}C_4H_5 + C_2H_2 \rightarrow \text{benzene} + H \quad (2)$$

The former, reaction 1, was suggested to play a key role in the formation of the first aromatic ring on the basis of detailed kinetic simulations of shock-tube acetylene pyrolysis,[4] the result reiterated in subsequent kinetic studies. These numerical simulations also identified reaction 2, suggested by Bittner and Howard,[5] as playing a role at lower temperatures.[6]

Reactions 1 and 2 were dismissed by Miller and Melius,[7] who suggested that n-C_4H_3 and n-C_4H_5 could not be present in sufficiently high concentrations because these radicals transform rapidly to their corresponding resonantly stabilized isomers, i-C_4H_3 and i-C_4H_5.

Past numerical analysis[8] revealed that Miller and Melius' conclusion on the C_4H_3 and C_4H_5 abundances originated primarily from the much lower stabilities predicted by BAC-MP4 for the n forms relative to the corresponding i forms of these radicals, which is especially pronounced in the case of the C_4H_3 isomers. The BAC-MP4 predictions for standard enthalpy differences between the n and i forms are 12 kcal/mol for the C_4H_5 isomers and 19 kcal/mol for the C_4H_3 isomers.[7] In contrast, the enthalpy differences in the initial kinetics studies of Frenklach *et al.*[4] were assumed to be about 8 kcal/mol, based on estimates of Benson. The 8 kcal/mol difference was incorporated into the group-additivity scheme of Stephen Stein, which served as a consistent thermodynamic set for the initial kinetic modeling.[4]

Recent quantum-mechanical studies report differences in the range of 7–14 kcal/mol for the n-C_4H_5 isomers,[9,10] and raised the standard enthalpy of formation of the n-C_4H_3 radical to 134 kcal/mol,[11] as compared to the previous estimates of 127[12] and 130[7] kcal/mol.

Our theoretical study,[13] employing the Diffusion Monte Carlo (DMC) method, resulted in 126.0, 119.4, 83.4, and 76.2 kcal/mol for the n-C_4H_3, i-C_4H_3, n-C_4H_5, and i-C_4H_5, respectively, all with one standard deviation of 0.6 kcal/mol. These results translate into the enthalpy differences of 6.6±1.2 kcal/mol for C_4H_3 and 7.2±1.2 kcal/mol for C_4H_5 radicals, substantially lower than the prior theoretical predictions. The DMC results suggest higher stability for the n radicals, bringing the difference between the n and i isomers essentially back to the Benson estimates. The higher stability of n-C_4H_3 and n-C_4H_5 predicted by DMC "restores" the importance of reactions 1 and 2.

Odd-Carbon-Atom Pathways

As an alternative to the even-carbon-atom pathways of forming the first aromatic ring, several investigators proposed an odd-carbon-atom pathway via combination of propargyl radicals

$$C_3H_3 + C_3H_3 \rightarrow \text{benzene or phenyl} + H \quad (3)$$

Indeed, the propargyl radical is an exceptionally stable hydrocarbon radical, and its implication to the formation of aromatics and soot has long been supposed. Quantum chemical calculations indicated that the chemical activation of the adduct might be sufficient in surmounting the numerous potential energy barriers to its cyclization to an aromatic ring. Other odd-carbon-atom pathways have been suggested,

$$C_5H_5 + CH_3 \rightarrow \text{benzene} + H + H \quad (4)$$

$$C_5H_5 + C_5H_5 \rightarrow \text{naphthalene} + H + H \quad (5)$$

Recent results of a time-dependent solution of the energy master equations[10] revealed a significantly lower rate for reaction pathway 3 as compared to the initial estimate[7] of 1×10^{13} cm^3 mol^{-1} s^{-1}; yet, the new theoretical values are consistent with those deduced by consistent modeling of experiment.[8,14] Support to the even-carbon-atom channels comes also from recent experimental studies.[15,16]

It is important to realize that focusing on the competition between reactions 1 and 3 confines one's scientific quest to a narrow point of view. It is shown, for instance, that with the increase in pressure, formation of the first aromatic ring via linear C_6H_x species begins to play a significant if not a dominant role, and so are ring-ring reactions. In this regard, it is pertinent to mention that formation of single-aromatic-ring compounds, while probably most common, may not necessarily be the rate-limiting step, and the growth of PAHs can be initiated by the direct formation of multi-ring PAHs, bypassing the formation of the benzene ring. Such proposals include formation of aromatics from "condensation" of polyacetylenes, combination of C_4H_x species, as well as combination of larger radicals (for an extensive list of references to the points mentioned above see Ref. 17).

Propargyl + Acetylene

Another possibility for the initial ring formation is the reaction between propargyl and acetylene forming a cyclopentadienyl radical,

$$C_3H_3 + C_2H_2 \rightarrow c\text{-}C_5H_5 \quad (6)$$

This pathway combines the benefits of the two reactant types discussed above: highly stable radical, propargyl, and the most abundant "building block", acetylene. Once formed, cyclopentadienyl reacts rapidly to form benzene. The possibility of a propargyl-acetylene reaction initiating formation and growth of aromatics was brought up in the past, as a possible explanation to an experimentally observed enhancement in the production of soot in shock-heated mixtures of benzene and allene.[18] Recent quantum Monte Carlo calculations along with time-dependent solution of the energy-transfer master equations demonstrated feasibility of this proposal.[19] Indeed, the equilibrium of reaction 6 at typical flame conditions is shifted to the right above 1700 K, implying the formation direction within the temperature window of aromatics formation. The predicted for these conditions (1 atm and 1500 K) rate coefficient is about 1×10^{11} cm^3 mol^{-1} s^{-1}. Let's compare then the rate of reaction 6, $k_6[C_3H_3][C_2H_2]$, with that of reaction 3, $k_3[C_3H_3][C_3H_3]$. Noting that $[C_3H_3]$ is canceled out and using the value of $k_3 = (1 \text{ to } 5)\times10^{12}$ cm^3 mol^{-1} s^{-1}, we obtain

$$\frac{k_6[C_3H_3][C_2H_2]}{k_3[C_3H_3][C_3H_3]} \sim (0.02 \text{ to } 0.1)\frac{[C_2H_2]}{[C_3H_3]} \quad (7)$$

The concentration ratio $[C_2H_2]/[C_3H_3]$ is on the order of 10^2–10^4 as reported in numerous experimental flame studies and hence reaction 6 is expected to be faster than reaction 3 by a factor of 2 to 10^3. This implies that reaction 6 is not just fast enough to make a difference, but probably should play a dominant role in formation of the first aromatic ring.

Acknowledgement. The authors wish to thank John Kiefer, Al Wagner, and Hai Wang for helpful discussions on the structure of the cyclopentadienyl radical. The research was supported by the Director, Office of Science, Office of Basic Energy Sciences, Chemical Sciences Division of the U.S. Department of Energy, under the contract number DE-AC03-76SF00098. Calculations were performed, in part, at the National Energy Research Scientific Computing (NERSC) Center.

References

(1) Hammond, B. L.; Lester, W. A., Jr.; Reynolds, P. J. *Monte Carlo Methods in Ab Initio Quantum Chemistry*; World Scientific: Singapore, 1994.
(2) Krokidis, X.; Moriarty, N. W.; Lester, W. A., Jr.; Frenklach, M. *Chem. Phys. Lett.* **1999**, *314*, 534.
(3) Barker, J. R. MultiWell; 1.1.1 ed., 2001.
(4) Frenklach, M.; Clary, D. W.; Gardiner, W. C., Jr.; Stein, S. E. *Proc. Combust. Inst.* **1985**, *20*, 887.
(5) Bittner, J. D.; Howard, J. B. *Proc. Combust. Inst.* **1981**, *18*, 1105.
(6) Frenklach, M.; Warnatz, J. *Combust. Sci. Technol.* **1987**, *51*, 265.
(7) Miller, J. A.; Melius, C. F. *Combust. Flame* **1992**, *91*, 21.
(8) Wang, H.; Frenklach, M. *Combust. Flame* **1997**, *110*, 173.
(9) Parker, C. L.; Cooksy, A. L. *J. Phys. Chem. A* **1999**, *103*, 2160.
(10) Miller, J. A.; Klippenstein, S. J. *J. Phys. Chem. A* **2001**, *105*, 7267.
(11) Cioslowski, J.; Liu, G.; Moncrieff, D. *J. Phys. Chem. A* **1999**, *103*, 11465.
(12) Wang, H.; Frenklach, M. *J. Phys. Chem.* **1994**, *98*, 11465.
(13) Krokidis, X.; Moriarty, N. W.; Lester, W. A., Jr.; Frenklach, M. *Int. J. Chem. Kinet.* **2001**, *33*, 808.
(14) Appel, J.; Bockhorn, H.; Frenklach, M. *Combust. Flame* **2000**, *121*, 122.
(15) McEnally, C. S.; Pfefferle, L. D. *Proc. Combust. Inst.* **2000**, *28*, 2569.
(16) Olten, N.; Senkan, S. *Combust. Flame* **2001**, *125*, 1032.
(17) Frenklach, M. *Phys. Chem. Chem. Phys.* **2002,** in press.
(18) Frenklach, M.; Yuan, T.; Ramachandra, M. K. *Energy & Fuels* **1988**, *2*, 462.
(19) Moriarty, N. W.; Krokidis, X.; Lester, W. A., Jr.; Frenklach, M. 2nd Joint Meeting of the U.S. Sections of the Combustion Institute, Paper 102, 2001, Oakland, CA.

Proof of the Transient Nature of Precursor Soot

Peter T. A. Reilly, Ryan P. Rodgers,
William B. Whitten and J. Michael Ramsey

Oak Ridge National Laboratory
PO Box 2008, MS 6142, Oak Ridge, TN, 37831

Introduction

For more than fifty years, scientists and engineers have attempted to model and understand the chemistry of mature soot formation through the chemistry of the gas phase without success as evidenced by the lack of any model with predictive capabilities. Until now, the chemistry of the condensed phase has been essentially ignored.

Yet the existence of a condensed phase other than mature soot has been know to exist in flames and other pyrolytic environments since 1950 when Parker and Wolfhard[1] observed the presence of precursor soot in flames. In 1956, the existence of precursor soot (a high temperature stable form of hydrocarbon) was conclusively proven by the observance of a white mist that formed in huge furnaces used for the industrial production of carbon black.[2] When the temperature of the furnace was raised, the mist became carbon black (mature soot).

Though this evidence was conclusive, the presence of precursor soot in combustion environments has been ignored and even denied by experts with the suggestion that sampling-induced condensation or dilution is the reason for observations of precursor soot. We have searched the literature for refutation of the existence of precursor soot but nothing was found. However, our search of the literature showed that the existence of precursor soot has resurfaced on a fairly regular basis over the last thirty years, first by the shock tube work of Graham and coworkers in the 1970's,[3] then in the 1980's by Miki et al.[4] during flow tube pyrolysis of fuels. Later Dobbins and others[5] demonstrated its presence in flames by TEM and thermophoretic sampling in the late 80s and early 90s. Subsequently, D'Alessio et al.[6] rediscovered precursor soot in flames using absorption, fluorescence and scattering measurements and finally our group directly observed the carbonization process using real-time aerosol mass spectrometry from an acetylene flame.[7]

Given the nature of the pyrolysis experiments performed by Swietzer and Heller in 1956 and the vehemence of the experts that suggest precursor soot is the result of sampling and dilution artifacts or only exists in minute amounts, we thought that it would be a good idea to establish hard physical evidence of the existence of precursor soot as well as develop a theory for its presence in combustion environments.

Furthermore, we noticed that there is a big difference between the mass spectra of the gas phase[8] and condensed species[9] of rich flames. We also realized that there have been no simultaneous measurements of the gas and condensed phases for an accurate comparison. Consequently, we decided to perform these measurements on fuel pyrolyzed in a flow tube reactor to maintain simplicity and reproducibility. For further comparison, we also decided to perform direct comparisons of our real-time measurements with off-line techniques.

Experimental

The experimental data shown here are only a part of a larger program for understanding the chemistry of precursor soot. Experiments have also been preformed at higher temperatures and by a variety of techniques, including electron impact ionization mass spectrometry, GCMS and laser desorption ionization mass spectrometry (LDMS).

Acetylene at atmospheric pressure with a small impurity of acetone was passed through a 3.85-mm ID 45-cm long quartz tube reactor at a constant temperature of 700 and 800 °C in two separate experiments. Miki et al.[4] obtained similar results during flow tube pyrolysis of a variety of hydrocarbons; therefore we suggest that the small acetone impurity did not significantly perturb our results. The flow through the reactor was laminar at a 40-ml/min flow rate. Immediately, upon exiting the reactor, the effluent was rapidly diluted one hundred fold with a 4-l/min flow of pure room temperature N_2. The diluted effluent was sampled directly into our ion trap based aerosol mass spectrometer. The configuration of this instrument has been described in detail elsewhere.[7]

Briefly, the diluted aerosol was sampled through a differentially pumped inlet that creates a collimated particle beam that passes through the center of the ion trap. On the way to the ion trap the particles were aerodynamically sized by light scattering based time-of-flight. When the detected particles reached the center of the ion trap, a focused pulse from an excimer laser (~ 1 J/cm^2) ablated and ionized the individual particles. The ablated ions were then mass analyzed by standard ion trap techniques. For each detected particle, we obtained the aerodynamic size and a mass spectrum.

Particle mass spectra were obtained by ablating each individual particle in real time as it passed through the ion trap. Gas phase mass spectra of the diluted effluent were obtained with the 308-nm laser whenever the laser "missed" the particle. The composition of the gas phase was checked by deliberately mistiming the laser to miss the particles as they passed through the trap. The composition of the gas phase was also examined by electron impact (EI) ionization with an ion collection time of 500 ms. The laser and electron impact mass spectra were comparable with the EI spectra showing subtle differences primarily in the degree of hydrogenation.

The diluted effluent was collected on hydrophobic polyvinylidene fluoride membrane filters (Millipore, 0.22-μm pore size) for further off-line analysis. The effluent was extracted from the filter with methylene chloride. The extractant was analyzed by several techniques. GCMS was used to identify the low mass components (< 300 Da). Laser desorption/ionization mass spectrometry (LDMS) was used to evaluate the high mass components (> 300 Da). The extracted effluent was also deposited on C18 coated 5-μm silica beads by solvent evaporation. These beads are standard packing for liquid chromatography columns. The beads were analyzed individually with our aerosol mass spectrometer by sprinkling them over the inlet thus yielding a direct comparison between real-time and off-line particle analysis.

Results and Discussion

Figure 1 shows the averaged mass spectra of the gas phase, the particle phase, and the filter collected effluent deposited on 5-μm C-18 coated silica beads to give a direct comparison of the gas phase species with the real-time and off-line analysis of the condensed species. Comparison of the gas (a) and real-time particle phase (b) averaged spectra reveal similar ion intensity patterns yet there are subtle and profound differences. There is an obvious broadening of the local mass distributions that is due to hydrogen exchange.[7] This is a condensed phase phenomenon. There is also a positive mass shift between the gas and condensed phases. Since atomic or molecular hydrogen does not condense at room temperature, the particles that we are observing have to be created in the reactor and not during the dilution step. The differences in the gas and particle phase compositions become more pronounced at higher temperatures.

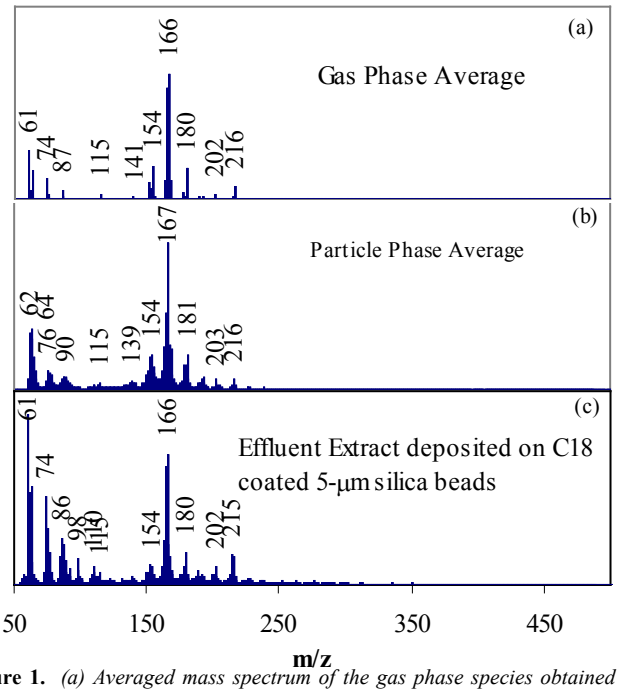

Figure 1. *(a) Averaged mass spectrum of the gas phase species obtained by mistiming the laser. (b) Averaged particle mass spectrum. (c) Averaged mass spectrum of the filter collected effluent deposited on 5-μm C18-coated silica beads and dropped into the particle mass spectrometer inlet for direct comparison of real-time and off-line measurements.*

Comparison of the real-time and off-line mass spectra shows that the particles that we sample in real-time have the same composition as the filter collected effluent with excess hydrogen. This means that we have a valid method for comparing real-time and off-line measurements. To demonstrate the volatility of the PAHs in the precursor soot at room temperature, we performed standard LDMS on the extractant deposited on a stainless steel probe. The solvent was allowed to evaporate and the before the probe was placed in vacuum. Figure 2 shows the averaged mass spectrum of the extractant. Comparison of Figures 1 (c) and 2 reveal that large quantities of the condensed species evaporate in vacuum before the measurements are made. This comparison clearly demonstrates the need for freezing the precursor soot samples before they are exposed to vacuum. This is particularly relevant to those people that do TEM and LMMS measurements on precursor soot.

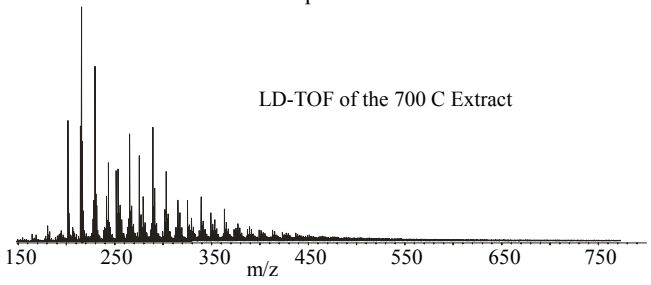

Figure 2. *Averaged laser desorption time-of-flight mass spectrum of the filter-collected extract deposited on a stainless steel probe.*

Ion traps are known to have a limited dynamic range. Consequently, high mass species have to be measured in separate experiments. Figure 3 (a) presents the averaged real-time mass spectrum of the high mass of the high mass species in the particles and Figure 3 (b) presents the averaged off-line mass spectrum of the high mass species from the filter extract deposited on the C-18 coated

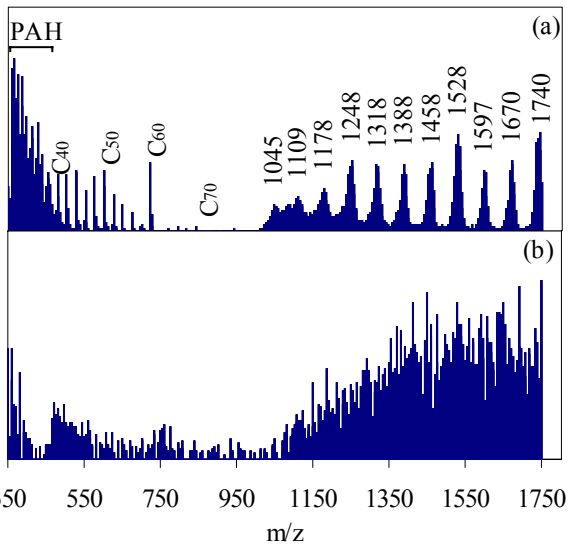

Figure 3. *(a) Averaged real-time high mass spectrum of the particle phase. (b) Averaged off-line high mass spectrum of the extract.*

particles. In the real-time mass spectrum (a), we observe the tail end of the PAH distribution on the left. Out of that distribution, we see a distribution of fullerenes emerge marked by a 24 u peak separation and the highest intensity at 720 u (C_{60}). At higher mass, we see an ion distribution that looks similar to that seen in the mass spectra of polymers. This distribution is marked by a peak separation of approximately 70 u (C_5H_{10}). This distribution has never been seen before. Comparison to the off-line mass spectra reveals scrambling of the high mass species and loss of the fullerene masses (fullerenes are not soluble in the C-18 matrix). The off-line LDMS spectrum from the same extract in Figure 2 was taken weeks later and reveals only digitizer noise above 1000 u. Species in the high mass region of the spectrum do not evaporate in vacuum. Consequently, our observed high mass species must be metastable. Since the only other species in the mass spectra are low mass PAHs and other small hydrocarbons, it seems likely that these high mass species have decomposed into the species observed in the low mass region of the spectrum. Our data proves the transient nature of precursor soot and suggests that the theory and experiments on soot formation need to be completely reexamined.

Acknowledgement. We thank Dr. Christopher L. Hendrickson for the LDMS work. This research was sponsored by the Division of Chemical Sciences, Office of Basic Energy Sciences, U.S. Department of Energy, under contract DE-AC05-00OR22725 with Oak Ridge National Laboratory, managed and operated by UT-Battelle, LLC.

References

1. Parker, W. G.; Wolfhard, H. G. *J. Chem. Soc. (London)* **1950**, 2038.
2. Sweitzer, C. W.; Heller, G. L. *Rubber World* **1956**, *134*, 855-865.
3. Graham, S. C.; Homer, J. B.; Rosenfeld, J. L. J. *Mod. Dev. Shock Tube Res., Proc. Int. Shock Tube Symp., 10th* **1975**, 621-31.
4. Miki, H.; Takeuchi, K.; Ishida, K.; Yoshihara, Y. *Bull. JSME* **1986**, *29*, 149-55.
5. Dobbins, R. A.; Subramaniasivam, H. *Chem. Phys. Processes Combust.* **1991**, 76-1/76-4.
6. D'Alessio, A.; D'Anna, A.; D'Orsl, A.; Minutolo, P.; Barbella, R.; Ciajolo, A. *Symp. (Int.) Combust., [Proc.]* **1992**, *24th*, 973-80.
7. Reilly, P. T. A.; Gieray, R. A.; Whitten, W. B.; Ramsey, J. M. *Combust. Flame* **2000**, *122*, 90-104.
8. Homann, K.-H. *Angew. Chem., Int. Ed.* **1998**, *37*, 2435-2451.
9. Tregrossi, A.; Ciajolo, A.; Barbella, R. *Combust. Flame* **1999**, *117*, 553-561.

SIZE EXCLUSION CHROMATOGRAPHY OF FUEL RICH COMBUSTION PRODUCTS

Barbara Apicella[1], Anna Ciajolo[1], Isabel Suelves[2], Trevor Morgan[3], Alan A., Herod[3], Rafael Kandiyoti[3]

1. Istituto di Ricerche sulla Combustione – CNR, P.le Tecchio, 80 – 80125 Napoli - Italy
2. Instituto de Carboquimica, CSIC, Miguel Luesma Castan 4, 50015 Zaragoza, Spain
3. Department of Chemical Engineering, Imperial College, Prince Consort Road, London, SW7 2 BY, UK.

Introduction

To control the emission of PAH and particulate carbon from combustion processes, it is necessary to know their formation mechanism. It is generally accepted that intact aromatic ring units like benzene and polycyclic aromatic hydrocarbons, commonly detected in the soot inception region, play an important role in soot formation[1]. However, the mechanism is far from being completely understood. High mass species have not been detected in the mass range between (i) typical PAH detected by chromatographic analysis (< 400u), and (ii) the first soot particles (>2,000 u).

The characterisation of high mass combustion products presents the same analytical difficulties encountered in the characterisation of complex carbon systems like coals and coal-derived materials[2-4]. In this study, similar, size exclusion chromatography based, methods have been used to characterize samples collected in two combustion systems, burning gaseous and liquid fuels under fuel-rich conditions.

Experimental

Equipment: Condensed species and soot samples were collected[5] from a premixed laminar gas flame and a fuel oil spray flame. The rich premixed ethylene/oxygen flame was produced on a McKenna burner at a fixed C/O ratio of 0.8. The spray flames were produced by atomising fuels in a 100 kW three-flux low-NOx burner inserted in a cylindrical vertical furnace of ceramic fibre (0.36 m ID and 2.5 m height). An aromatic-free vegetable oil (rapeseed oil) and three commercial fossil fuels (heavy fuel oil, diesel oil and kerosene), with different aromatic contents, were used as fuels.

A stainless-steel water-cooled probe was used to sample combustion products along the flame axis. Solid and condensed material collected on the probe wall, on the teflon filter and in an ice-cooled trap in the sampling line were extracted by dichloromethane (DCM) to separate condensed species (CS) soluble in DCM, from 'solid' carbonaceous material (soot), insoluble in DCM.

The CS-fraction and the soot were dried, weighed and dissolved in N-methyl-2-pyrrolidinone (NMP) for examination by size exclusion chromatography (SEC).

Size exclusion chromatography: The chromatographic system has been described previously[6-7]. Two different SEC columns have been used in the study, both packed with polystyrene-polydivinylbenzene beads (Polymer Laboratories, UK). The 'Mixed-D' column was packed with 5 μm nominal dia beads and the 'Mixed-A' column with 20 μm nominal dia beads. The Mixed-D column was operated at 80°C with an NMP flow rate of 0.5 mL min^{-1} and connected to two detectors. A Perkin-Elmer LC 290 variable wavelength UV-absorbance cell set at 450nm and an Applied Biosystems diode array detector set at at 280, 300, 350, 370 and 450 nm were used to characterise the samples in solution. The linear operating range of the 'Mixed-D' column was from low mass (100u) up to 200,000 u (the exclusion limit). A different nearly linear relationship was found between log10 molecular mass and elution time, above 200,000.

The Mixed-A column was connected to a Knauer WellChrom Microstar K-120 HPLC pump with an evaporative light scattering detector (Polymer Laboratories ELS 1000) and operated at room temperature with a flow rate of 0.5 ml min-1. The Mixed-A column has a linear range between log10 molecular mass and elution time extending to higher masses, up to polystyrene standard of mass 15 million u, the largest oligomer available in this work.

Results and Discussion

In this work, NMP was used not only as an eluent but also as a solvent for the combustion products. All the species soluble in DCM dissolve very well in NMP, but another important property of NMP is the capability to give stable suspensions (solutions?) of soot, analysable by the two SEC systems. The attribution of a molecular mass to a specific retention time has been made on the basis of calibration curves using polystyrene standards. Calibration curves for the two columns (A and D) have been presented elsewhere[3-4, 8].

On the first system (Mixed-A column with ELS), as shown in soot gives a SEC chromatogram with an unique sharp peak at 10.5 min (Fig 1).This corresponds to a molecular mass above 100,000,000 u, if evaluated by extrapolating the calibration curve. Clearly, this is a hazardous procedure; the masses are very high and well above the exclusion limit of the column. Were these MMs taken at face value, they would correspond to soot dimensions of about 100nm.

Figure 1 also shows the chromatogram of the CS-sample with a bimodal distribution, with peaks centered around 14 and 21 min. GC-ms analyses of the CS-fractions from all samples used in our study show that PAH with molecular mass up to 300 u ('GC-MS PAH') constitute a proportion of the samples between 30 - 50 % by weight.

In Figure 1, the peak at 21 min comprises lower MW material in the GC-MS range and extending up to several thousand of u. The material in the upper MW range (peak at 14 min) corresponds to a MMs between 1,000,000 u and 10,000,000 u. It is presumed they have different conformations than the lower mass material. These differences are not understood but may reflect a change from planar or near-planar structures of the material accessible to GC-MS analysis to three-dimensional structures. The higher mass species are thought to be the precursors of soot. Here we have only shown the chromatograms of products from the ethylene flame[8]; chromatograms from the other fuels were similar.

Using the second system (Mixed D column with uv-absorption detector) it is possible to have better resolution at lower MMs.

Mixed-D soot chromatograms for diesel oil, rapeseed oil and ethylene showed three peaks at 6, 8 and 10 min (Fig.2). The higher value, which corresponds to a molecular mass between 100,000,000 u <1,000,000,000 u, is similar to that evaluated by using the Mixed-A column with the ELS detector. It corresponds to 100nm soot particles, but it is above the exclusion limit of the column and above the largest molecular mass standard, as evaluated by polystyrene calibration. Moreover, the peaks at 8 and 10 min signal the presence of intermediate size material of about 20nm characteristic dimension (10,000,000 u) and less than 10nm (100,000 u), respectively.

The chromatograms of heavy fuel oil soot and of the kerosene soot have not been shown in Fig 2; the first one almost completely overlapped with diesel oil soot and the second with the ethylene soot.

These results indicate that SEC chromatograms of soot do not change significantly, when the physical state (gaseous for the premixed flame and liquid for the spray flame) or the chemical composition of the fuels (ethylene gas, rapeseed oil, kerosene, diesel oil and heavy fuel oil) are changed.

The common strand seems to be the operation in a fuel rich combustion regime.

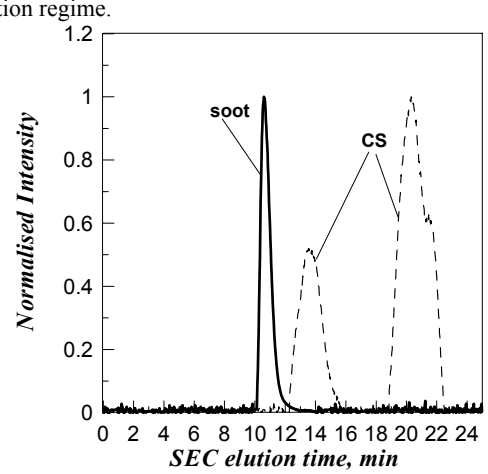

Figure 1. SEC chromatograms of ethylene soot and CS on Mixed A column.

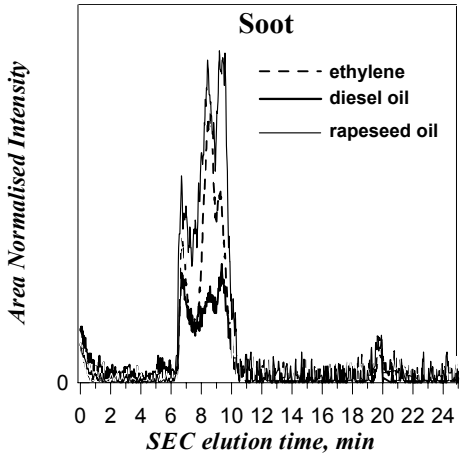

Figure 2. SEC chromatograms of soot from different fuels on Mixed D column.

The Mixed-D SEC chromatograms of ethylene, kerosene and diesel oil CS shown in Fig.3 present four peaks at 9, 10, 18 and 20 min. The first two peaks correspond to molecular masses of 1,000,000 u and 300,000 u, respectively. The small peak at 18 min corresponds to 1000 u and the large peak at 20 to about 200-300 u. The latter corresponds to the molecular mass of the 'GC-MS PAH'. This attribution confirms that only a fraction of the CS-fraction is composed of PAH from two to seven rings. The heavy fuel oil CS and the rapeseed oil CS chromatograms (not reported) give peaks exactly in the same region of the other fuels. As in the case of soot, the molecular mass distributions of the CS-fractions appear to be independent of the combustion systems and of the fuels. These observations were made using a highly selective PL-gel Mixed D column with UV-visible absorption detection.

Clearly, molecular masses at or above exclusion limits of the columns can be only considered as semi-quantitative approximations. However, the agreement between the magnitudes of the masses observed by the two techniques (Mixed Mixed-A column with a light scattering detector and Mixed –D column with a UV-visible diode array detector) suggests these values may be treated as good estimates. The similarities between properties of the soot clearly show that their properties depend primarily on the combustion regime.

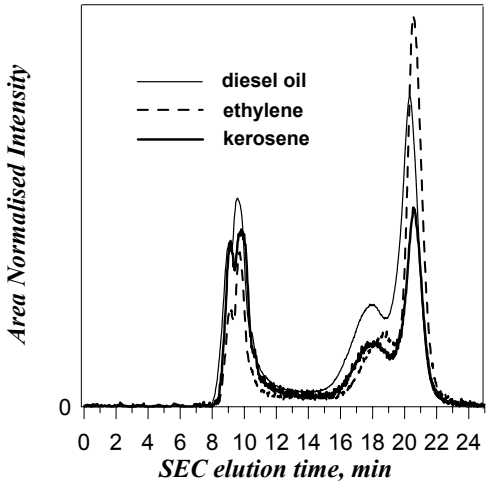

Figure 3. SEC chromatograms of CS from different fuels on Mixed D column.

Conclusions

The evidence from this work indicates that soot is composed by large entities, which appear to be molecular rather than aggregates of small molecules. We have observed step-changes in structures from the small near-planar PAH molecules, present in the CS, to large components equivalent to polystyrenes of mass about 100,000 - 1 million, present both in the CS and in the soot, and to the very large particles of diameter greater than 20 nm.

The solution chromatography of soot provides a path to a more complete characterisation than has been hitherto possible.

Another important result of this work is that all the soot and Condensed Species soluble in DCM present the same molecular mass distribution, irrespective not only of combustion system, but also of the fuel used, even though fuels with very different chemical and physical characteristics have been combusted.

References

(1) Haynes, B.S. and Wagner, H. Gg., *Prog. Energy Combust.Sci,.* **1981**,7, .229-273.

(2) Herod, A. A., Lazaro, M., J., Shearman, J., Card, J., Jones, A., R., Kandiyoti, R., *Fuel,* **1999,** 78, 861-.

(3) Herod, A. A., Lazaro, M., J., Suelves. I., Dubau, C., Richaud,, R., Shearman, J., Card, J., Jones, A., R., Kandiyoti, R., *Energy & Fuels,* **2000,** 14, 1009-1020.

(4) Herod, A. A., Lazaro, M., J., Domin, M., Islas, C., A., Kandiyoti, R., *Fuel,* **2000,** 79, 323-.

(5) Ciajolo, A., D'Anna, A., Barbella, R., Tregrossi, A., Violi, A., *Proceeding of 26st Symposium (International) on Combustion, The Combustion Institute, Pittsburg,* **1996,** 2327-.

(6) Domin, M., Herod, A. A., Kandiyoti, R., Larsen, J. W., Lazaro, M. J., Li, S., Rahimi, P., *Energy & Fuels,* **1999,** 13, 552-.

(7) Herod, A. A., Zang, S., F., Johnson, B., R., Bartle, K., D., Kandiyoti, R., *Energy & Fuels*, **1996,** 10, 743-.

(8) Apicella, B., Ciajolo, A., Suelves, I. Morgan, T., Herod, A.A., Kandiyoti, R., *Proceedings of the Second Mediterranean Symposium on Combustion,*Sharm el Sheik, **2002**.

SMALL-ANGLE X-RAY SCATTERING FOR STUDIES OF SOOT INCEPTION AND FORMATION

Jan P. Hessler, Soenke Seifert, and Randall E. Winans

Chemistry Division
Argonne National Laboratory
9700 South Cass Avenue
Argonne, Illinois 60439-4831

Introduction

A comprehensive model that is capable of predicting the inception and growth of soot over a wide range of chemical and physical conditions is just beginning to emerge and has been documented in various workshops[1] and symposia[2]. In general, *in situ* measurements of soot have been performed with light in the ultraviolet, optical, and infrared regions and include absorption[3], induced[4] and natural[5] incandescence, and wide-angle elastic scattering[6]. Scattering measurements provide information on the morphology of particles that are larger than 15 nm while absorption and incandescence has been used to detect particles with mean radii between 1.8 and 10 nm. Small-angle x-ray scattering (SAXS) is ideally suited to provide *in situ* measurements in the important region between 1 and 100 nm[7].

In 1986 W. A. England presented the first *in situ* SAXS studies of soot.[8] He used a second-generation x-ray source and his exposure times had to be quite long. Third-generation x-ray sources, such as the Advanced Photon Source at Argonne National Laboratory, contain insertions devices, in our case an undulator, that increase the spectral brilliance of the x-rays by as much as a factor of 5000 compared to a bending magnet.[9] Because of this dramatic increase in brilliance only a few seconds are needed to obtain a scattering profile from soot particles formed in a flame. Recently, we reported our first SAXS measurements of soot formation.[10]

We observed numerous "dips" in the scattering profiles that could not be explained with standard calculations or models. Here, we present new and more detailed measurements that allow us to identify and extract a spatially dependent background, which we attribute to a temperature/density gradient that is produced by the flame front, and the axial and radial dependence of the scattering profiles. These profiles indicate at least a bimodal distribution of soot particles. The larger particles of this distribution correspond to poly-dispersed primary particles whose morphology depends critically upon the axial and radial position within the flame. In particular, at and above the widest part of the flame we observe three distinct radial regions. Near the center of the flame the mean value of the radius of gyration of the primary particles is relative small, e.g. 10 nm or less, and the polydispersity is significant, e.g. ~ 0.3. Beyond this region is a transition region where the mean radius of gyration increases by about a factor of two, e.g. to 21 nm, and the polydispersity decreases to ~ 0.2. Beyond the transition region the morphology of the primary particles is relatively constant, but the concentration changes significantly. At the present time we can not uniquely identify the smallest feature in the scattering profiles. This feature may be due to soot nuclei observed by di Stasio[11], polycyclic aromitic hydrocarbons such as naphthalene[12], or disordered carbons with graphitic basal planes[13].

Experimental

The SAXS instrument was constructed at ANL for use on the Basic Energy Sciences Synchrotron Radiation Center beamline ID-12-C at the Advanced Photon Source.[14]

X-rays produced in an undulator (6.0 –18.0 keV) pass through a double-crystal monochromator ($\Delta E/E \sim 10^{-4}$) and a focusing mirror. Typically, 10^{12} x-rays per second are incident on the flame. The fuel, e.g. toluene, acetylene, propylene, or ethylene, is injected into the center of a 25.4 mm by 25.4 mm flat-flame burner that supports either a methane/hydrogen/air flame or a diffusion.[15] A stable cylindrical flame that shows incandescence up to a height of approximately 100 mm is produced by adjusting the various flow rates. The scattered x-rays are detected by a nine-element mosaic CCD detector (150 mm by 150 mm) with a maximum resolution of 3000 x 3000 pixels.[16] A scattering profile is generated by subtraction the dark current, correcting for different pixel efficiencies, and averaging over the azimuthal angle. These profiles represent the differential scattering cross section, often called the scattering intensity, which is displayed as a function of the transferred momentum, $q = (4\pi/\lambda)\sin(\theta/2)$ where θ is the scattering angle and λ is the wavelength of the x-rays. At each of several heights above the burner one-hundred-thirty-six profiles are obtained as a function of the distance from the center of the flame. Two linear translation stages are used to move the flame horizontally and vertically with respect to the x-ray beam.

Results and Discussion

Spatially Dependent Contrast. One of the main challenges in performing small-angle x-ray scattering experiments is to subtract the scattered background from the observed scattering profile. When dealing with solid or liquid samples, this subtraction may be straightforward. However, when studying gaseous systems that are undergoing combustion, a temperature gradient, which is always present, produces a spatially dependent background. An example of a spatially dependent scattering intensity at a fixed value of transferred momentum such is shown in figure 1 below.

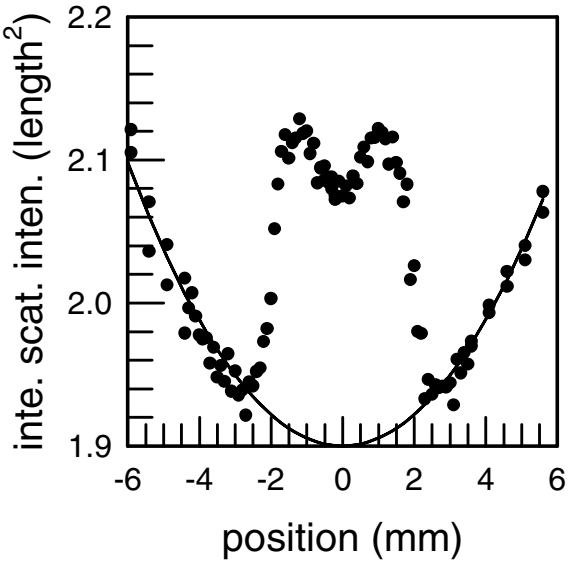

Figure 1. Measured scattering intensity at a fixed values of the transferred momentum as a function of laboratory position. The solid line is a parabola that reproduces the spatial dependence of the background scattering.

Radial Dependence of Scattering Intensity. Once the background has been subtracted we use the cylindrical symmetry of our flame to invert the measured profiles and, thereby, obtain the radial dependence of the scattering intensity.[17] One of the more

interesting spatially dependent observations involves scattering from primary soot particles in the region $0.1 < q(nm^{-1}) < 0.6$. In this region scattering is most easily discussed by generation a Porod plot[10], $\log\{q^4I(q)\}$ vs . $\log\{q\}$, which amplifies subtle changes in the scattering intensity. Figure 2 shows a series of Porod plots of the local scattering intensity for radial positions between 0.9 and 1.3 mm. The strongest profile clearly show a dip near 0.35 nm^{-1}. The location of this dip indicates that these particles have a mean radius of gyration of about 10 nm. The magnitude of the dip indicates that they are polydispersed with a polydispersity, $\sigma/\langle R_g \rangle$, ~ 0.3. Here, we have assumed that the particle distribution may be approximated by a Schultz distribution, which is supported by thermophoretic samples taken on this flame and analyzed by transmission microscopy[18]. The profile at a radial distance of 1.3 mm has three distinct dips at 0.2, 0.4, and 0.6 nm^{-1} This implies that the particles are about a factor of two larger. Here they are less dispersed with a polydispersity of 0.2.

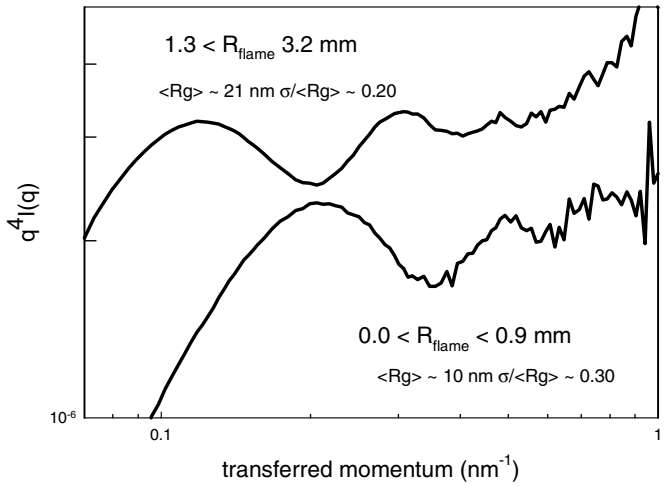

Figure 2. Porod plots of the local scattering intensity at distances of 0.9 and 1.3 mm from the center of the flame. Between 0.9 and 1.3 mm the profiles systematically change from one to the other.

The relative concentrations of the two species may be obtained by calculating the Porod invariant[10], which are shown in figure 3.

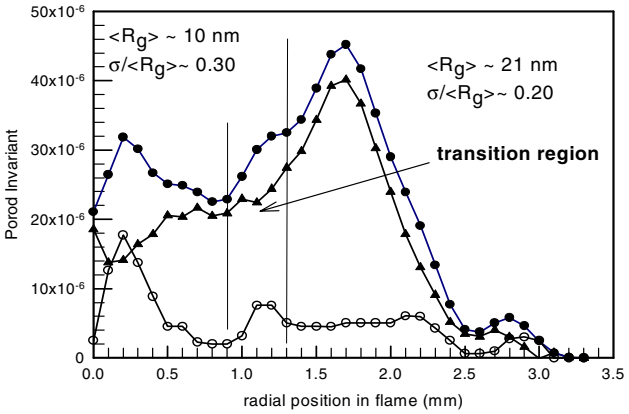

Figure 3. Porod invariant for different species. The solid circles represent the total concentration of soot species, the solid triangle represent the concentration of primary particles, and the open circles represent small species.

Here we note a a well defined transition region that increases in width as we move higher in the flame.

Conclusions

From the illustrations given here we see that SAXS provides a detailed description of the soot formation process that can not be obtained by other techniques. The challenge for the immediate future is to extend the range of SAXS in the gas phase from a transferred momentum of 1 nm-1 out to where diffraction peaks[13] have been observed, q ~ 10 nm^{-1}.

Acknowledgement. This work would not have been possible without the help of the staff of the Basic Energy Sciences Synchrotron radiation Center at Argonne's Advanced Photon Source, in particular, Mark A. Beno, Jennifer A. Linton, Mark S. Engbretson, and Guy Jennings. Helpful conversation with Albert F. Wagner and Stephen T. Pratt are gratefully acknowledged. This work was performed under the auspices of the U.S. Department of Energy, Office of Basic Energy Sciences, Division of Chemical Sciences, Geosciences, and Biosciences and use of the Advanced Photon Source was supported by BES-DOE all under contract number W-31-109-ENG-38.

References

(1) Bockhorn, H. , Ed., *Soot Formation in Combustion, Mechanisms and Models,* Springer-Verlag, Berlin, 1994.
(2) Homann, K.H.; Wornat, M. J., co-chairs of the colloquium on soot formation and destruction, *Proc. Comb. Inst*. **2000**, *28*, 2507-2658.
(3) Weiner, A. M.; Harris, S. J., *Combust. Flame* **1989**, *77*, 261.
(4) Woiki, D.; Giesen, A.; Roth, P. *Proc. Combust. Inst*. **2000**, *28*, 2531.
(5) Parker, T.E.; Morency, J.R.; Foutter, R.R.; Rawlins, W.T. *Combust. Flame* **1996**, *107*, 271.
(6) Di Stasio, S.; Massoli, P.; Lazzaro, M. *J. Aersol. Sci*. **1996**, *28*, 897.
(7) Williams, C.E.; May, R.P.; Guinier, A. In *X-ray Characterization of Materials*, Lifshin, E., Ed., Wiley-VCH, Weinheim, 1999, pp. 211-254.
(8) England, W.A. *Combust. Sci. Technol*. **1986**, *46*, 83.
(9) Arndt, U.W. In *International Tables for Crystallography, Volume C*, Wilson, A.J.C., Ed., Kluwer Academic Pub. Dordrecht, 1992, pp. 172-175.
(10) Hessler, J.P.; Seifert, S.; Winans, R.E. *Faraday Discuss*. **2001**, *119*, 395.
(11) Di Stasio, S. *Carbon*, **2001**, *39*, 109.
(12) VanWermeskerken, N.; Hessler, J.P.; Seifert, S.; Winans, R.E. private communication.
(13) Chen, H.X.; Dobbins, R.A. *Combust. Sci. Tech*. **2000**, *159*, 109.
(14) Seifert, S.; Winans, R.E.; Tiede, D.M.; Thiyagarajan, P. *J. Appl. Crystallogr*. **2000**, *33*, 782.
(15) Ma, J.; Fletcher, T.H.; Webb, B. *Energy Fuels* **1995**, *9*, 802.
(16) Naday, I.; Ross, S.; Westbrook, E.M.; Zenti, G. *Opt. Eng*. **1998**, *37*, 1235.
(17) Dasch, C.J. *Appl. Opts*. **1992**, *31*, 1146.
(18) Lee, K.O., private communication.

SOME ISSUES ON THE DEVELOPMENT OF A KINETIC MODEL FOR PAH FORMATION FROM HEPTANE COMBUSTION

Wing Tsang

National Institute of Standards and Technololgy
Gaithersburg, MD 20899

Introduction:

There has been considerable recent interest in the development of kinetic models for the simulation of the combustion of more realistic fuels[1-4]. Heptane is probably the simplest of such compounds and the present report deals with our attempts at describing the detailed kinetics of the decomposition of this fuel in the context of PAH and soot formation. Most detailed models of soot formation and indeed experimental studies begin with unsaturated compounds[5-7]. Others focus on the oxidation chemistry where soot formation precursors may not be even formed. In this paper we wish to call attention to the necessity of including the cracking chemistry or the breakdown of the larger hydrocarbon fuels in the database. When broken down into smaller unsaturated fragments they form the boundary conditions for existing soot formation databases. In addition we demonstrate new tools and procedures for the development of the database. These are of general applicability and are only gradually being applied to other aspects of PAH and soot formation.

Background:

The combustion of any fuel is initiated by the breakdown of fuel molecules to radicals[8]. These initial processes may lead to molecules containing a smaller number of carbon atoms than the fuel if the temperature is high or be of the same size if they are formed via attacks by radicals. All these radicals must now be broken down either through thermal decomposition or oxygen attack. Ultimately, one has a pool of smaller organics that can either be oxidized or under rich conditions oligomerize leading to PAH and soot. For the oxidation of small organics GRIMECH[9] is the widely used standard. We have mentioned the development of databases for soot formation from small unsaturated compounds. Our analysis of the literature indicate need for better definition of the cracking reactions. The present work is a report of our efforts in this area.

Pyrolytic decomposition involves the breakdown of stable fuel and olefins and the radicals that are formed as a result of these processes. For stable compounds rate constants can be readily estimated[10]. There is much less information on radical decomposition and is the focus of the present work[11]. Particular attention will be paid to the decomposition and isomerization of the heptyl radicals. Indeed it is the contribution of the latter that represents a particularly uncertain element[12]. The general situation is made more confusing by the low barriers for reaction of these processes. This leads to very large rate constants. As a result the usual Boltzmann distribution of reactants are disturbed and rate constants may be pressure dependent. We have recently formulated a procedure for the treatment of data for such[13-15] systems. It involves the determination of the distribution function for each isomer and then determining rate constants by convoluting it with the RRKM specfic rates [16]. Accurate values are required since the interest is in the competition with oxidation process and the pattern of unsaturated compounds must be properly specified in any kinetic database describing soot formation. In this work we will focus on the first breakdown step in the decomposition of the heptyl radicals. The processes of interest are summarized in Figure 1.

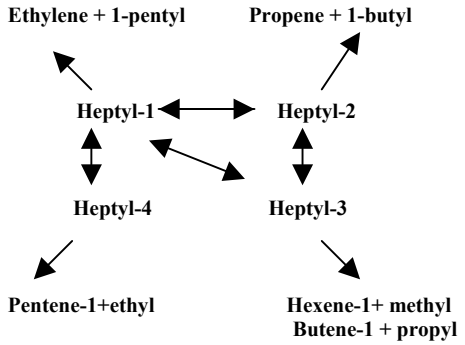

Figure 1 : Reaction channels in the decomposition of heptyl radicals

Experimental:

the yields of the 1-olefins can be found in Figure 2.Quantitative information on heptyl radical decomposition was obtained from single pulse shock tube experiments[17] on the decomposition of n-heptyl iodide. The weakness of the C-I[11] bond ensures that large quantities of 1-heptyl radicals will be released into the system. It can then undergo the thirteen possible reactions implied in Figure 1. Reactions were carried in large excesses of a radical scavenger, mesitylene so that all the radicals generated in the course of the reaction cannot react with the n-heptyl iodide or the decomposition products. Results in terms of branching ratios for olefin formation.

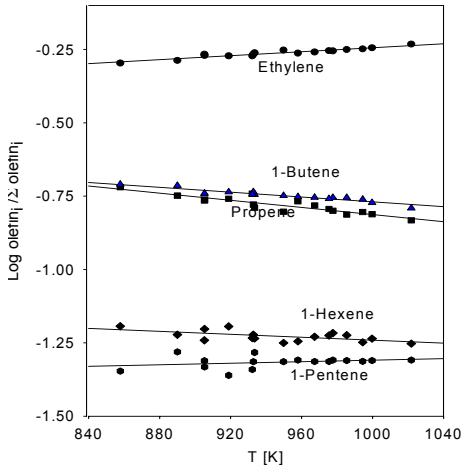

Figure 2: Branching ratios for the decomposition and isomerization of heptyl-1

Data Analysis:

The aim of this work is to reproduce the results in Figure 1 through the determination of the high pressure rate expressions for the reactions in Figure 1. Input data for the derivation of rate expressions are the thermodynamic properties of the isomers and the rate expression for beta bond cleavage. These were obtained from an analysis of the literature and taking into account the earlier recommendations on the proper manner for making estimates where data is absent{18-20]. The input and derived rate expressions can be found in Table 1. The derived rate expression for the 1-4 and 1-5

.

Reactions	A-factor s^{-1}	Activation Energy Kcal/mol
C_7H_{15}-1=C_2H_4+C_5H_{11} [1]	**$1.55x10^{13}$**	**27802**
C_7H_{15}-2=C_3H_6+C_4H_9 [2]	**$2.04x10^{13}$**	**27627**
C_7H_{15}-3=1-C_4H_8+C_3H_7 [3]	**$2.04x10^{13}$**	**27527**
C_7H_{15}-3=1-C_6H_{12}+CH_3 [4]	**$1.25x10^{13}$**	**29018**
C_7H_{15}-4=1-C_5H_{10}+C_2H_5 [5]	**$5.0x10^{13}$**	**27820**
C_7H_{15}-2= C_7H_{15}-1 [a]	$1.19x10^{11}$	20594
C_7H_{15}-3= C_7H_{15}-1 [b]	$5.93x10^{11}$	19758
C_7H_{15}-4= C_7H_{15}-1 [c]	$3.03x10^{12}$	25508
C_7H_{15}-2= C_7H_{15}-3 [d]	$7.99x10^{11}$	23748
C_7H_{15}-1= C_7H_{15}-2 [e]	$1.13x10^{13}$	17392
C_7H_{15}-1= C_7H_{15}-3 [f]	$7.31x10^{11}$	16738
C_7H_{15}-1= C_7H_{15}-4 [g]	$3.04x10^{12}$	22296
C_7H_{15}-3= C_7H_{15}-2 [h]	$7.93x10^{11}$	23749

Table 1. Rate expressions used to fit results in Figure 2.
Step size down was 500 cm^{-1}. Bold numbers are estimated rate expressions.

hydrogen shifts are consistent with earlier studies on the isomerization and decomposition of 1-pentyl (21) and 1-hexyl radicals(22).

With these high pressure rate expressions it is now possible to derive rate constants for all temperatures and pressures. Figure 3 contains a plot of rate constants as a function of time at 1200 K and 2 bar for 1-heptyl decomposition. It can be seen that they vary with time. The initial rate constant for 1-heptyl decomposition is a reflection of the thermal distribution at that temperature. Thus it is the high pressure rate constant. Here we are making the assumption that the initial 1-heptyl radical is created with a distribution that is appropriate to the bath temperature. The rate constant for all the other processes also have the same behavior. However the initial rate constant is not that the high pressure value. Indeed it is larger. The decomposition of the initial isomerization products are from a non-equilibrium distribution consisting of excited molecules that have just passed over the reaction barrier. Subsequent all the rate constant relax to a fairly constant value. This is the new steady state distribution with which the usual pressure dependent distribution functions can be derived.

An important problem with these results can be seen in the second figure in Figure 4. This contains the temporal behavior of the four radicals in question. It can be seen that at this temperature considerable reaction occurs during the time when the rate constants are varying with time. Thus rate constants derived from the steady state distributions can be expected to be in error. The issue arises as to the proper way to treat systems where rate constants are not constant. A possible approach is to note that these pathological situations occur when rate constants are very large. Under such conditions the actual values of the rate constants may not be important and all that are needed are the branching ratios. Figure 4 shows branching ratios as a function of time for the product yields from the four heptyl radicals formed as a consequence of 1-heptyl decomposition. It can be seen that all the channels make contributions. The most important is the products derived from the 3-heptyl radical. This is formed as a result of 1-5 hydrogen

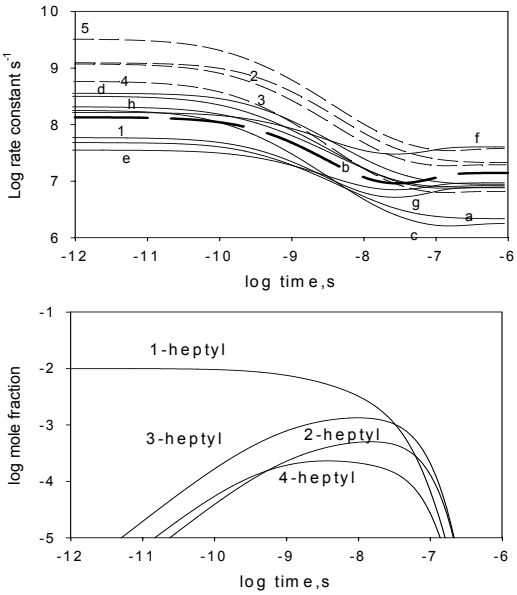

Figure 3: Top: Rate constants as a function of time at 1200 K and 2 bar based on the decomposition of 1-heptyl (long dashed line) . Short dashed lines are for other C-C bond fission. Solid lines are for isomerization. Numbers and letters for reactions in Table1
Bottom: Concentration as a function of time.

migration. This is the most likely isomerization process since it proceeds through a strain free six membered complex. There is a pressure dependence. However it is relatively small. A similar calculation beginning with any of the secondary radicals leads to the products from that radical being the predominant channel. For these cases the very small yields of products from the primary radical is a reflection of the equilibrium constants favoring the secondary radical by a factor of approximately 4. In the case of the 2 and 3 heptyls the second most important channel are products from the other radical. This is due to the contributions from the 2-3 hydrogen migration. It is however not fast enough the equilibrate the system. In the case of decomposition from the 4-heptyl, the contributions from the other channels are less than 5%.

Discussion:

An important issue is the condition for which the branching ratio information will be sufficient. Clearly this will be controlled by the nature of the competing process. For the present application this will be the reaction of the heptyl radicals with oxygen molecules in a combustion system. The initial process involve addition to form a peroxyl type radical. A characteristic rate constant is of the order of 10^{12} $cm^3mol^{-1}s^{-1}$ independent of temperature At 1 bar molecular oxygen concentration is $2x10^{-6}$ mol/cm^3 at 1000 K. Since the combination process can be reversed then actual conversion to oxygenated products can be assumed to be somewhat smaller. The consequence is that a unimolecular rate constant for heptyl decomposition 10^6 s^{-1} can be considered as a rough boundary. From the calculations it would appear that for a stoichiometric mixture 900 K would be an effective lower boundary above which the reactions of the heptyl radicals with oxygenare less important. It will be noted that below this temperature the reactions are only a factor

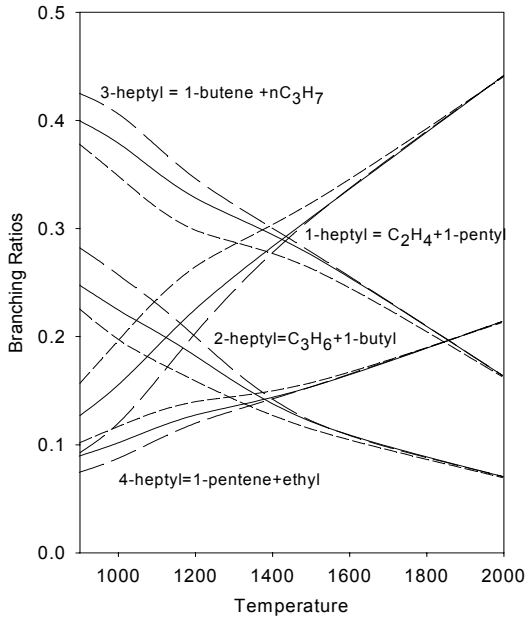

Figure 4: Branching ratio for the decomposition of the 4 isomeric heptyl radicals from 900 to 2000 K during 1-heptyl decomposition Branching ratio for the reaction 3-heptyl=methyl+1-hexene parallels that for 3-heptyl=1-butene+ nC_3H_7. The long dashed lines are at 20 bar. The solid lines are at 2 bar and the short dashed line are for 0.2 bar.

of 2 below the high pressure limit. Most of the decomposition is occurring in the steady state regime. Thus through the use of an arbitrary cut off it will probably be possible to get around the problem of rate constant not being constant.

The decomposition of the olefinic radicals formed from the olefin products in heptyl radical decomposition can be treated in a similar fashion. The added complexities are the possibility of cyclization leading to cyclopentyl and cyclohexyl type radicals and the formation of resonance stabilized allylic type radicals. These will include butadiene precursors. Initial inspection of available data suggests that the cyclic radicals will not be important products. Thus the cracking reactions will reduce heptane to a mixture of unsaturated compounds with up to four carbon atoms. It will then be possible to merge these results with the existing soot PAH forming and soot model as well as oxidation models to give a complete database for heptane combustion over wide ranges of stoichiometries. However we note that for the treatment of the larger molecular systems as in PAH formation, the procedures used here to take into account isomerization and energy transfer effects have not yet been applied. It may therefore be necessary to fine tune those databases.

Acknowledgement
This research was supported by the U.S. Department of Defense, through the Strategic Environmental Research and Development Program (SERDP # 1198), Charles Pellerin, Scientific Officer.

References
1. Curran, H.J., Gaffuri, P., Pitz, W.J., Westbrook, C.K. A comprehensive Modeling Study of n-Heptane Oxidation. Combust.Flame, 114:149-177 (1998). (preprint, of LLNL, 1997, UCRL-JC-126789).
2. Lindstedt, R.P., Maurice, L.Q. Combust.Sci.Tech., 1995, 107: 317-353.
3.. Bakali, A.E., Delfau, J-L., Vovelle, C., 1999, 118:381-389.
4. Fournet, R., Warth, V., Glaude, P.A., Battin-Leclerc, F., Scacchi, G., Come, G.M.,. Int.J.Chem.Kinet., 2000, 32:36-51.
5. Richter H, and Howard J.B., Prog. Energ. Combust.: 4 565, 2000
6. Frenklach, M., Clary, D.W., Yuan, T. , Gardiner, W. C., and Stein, S. E., Comb. Sci. and Tech., 50,79, 1986
7.. Marinov N.M., Castaldi M.J., Melius C.F., Tsang W., Comb. Sci. Tech., 128: (1-6) 295 1997
8. Griffiths, J. F. and Barnard, J. A. "Flame and Combustion", Blackie Academic, London, 3rd Edition, 1995
9. Smith, G. P., Golden, D. M., Frenklach, M., . Moriarty, N. W., Eiteneer, B., Goldenberg, M., Bowman, C. T., Hanson, R. K., Song, S., Gardiner, W. C., Jr., Lissianski, V. V., and Qin, Z., http://www.me.berkeley.edu/gri_mech/
10. Tsang, W., and Kiefer, J. H., "Unimolecular Reactions over Extended Pressure and Temperature Ranges" in Dynamics and Kinetics of Small Radicals, ed. K. Liu and A. Wagner. World Scientific Company, Singapore pg 59, 1995
11. Tsang, W., "Shock Tube Studies on the Stability of Polyatomic Molecules and the Determination of Bond Energies" in "Energetics of Stable Molecules and Reactive Intermediates" (Piedade, M. E. M., and Simoes, J. A. M., ed.) NATO Science Series Vol 535 , Kluver, Dordrecht, The Netherlands pg 323, 1999
12.. Frey, H. M., Walsh, R., Chem. Rev., 69, 103, 1969
13. Tsang, W., Bedanov, V. and Zachariah, M. R., J. Phys. Chem., 1996, 100, 4011.
14 Tsang, W. , Bedanov., V and Zachariah, M. R., Berichte der Busen-Gesellschaft fur Physikalische Chemie, 1997,101, 491.
15. Tsang, W., "A Pre-processor for the Generation of Chemical Kinetics Data for Simulations" AAIA-2001-0359, 39th AIAA Aerospace Sciences Meeting and Exhibit, Jamuary 8-11, 2001 Reno. NV
16 Gilbert, R. S. and Smith S. C.,"Theory of Unimolecular and Recombination Reactions", Blackwell Scientific, London, 1990
17. Tsang, W. and Lifshitz, A., "Single Pulse Shock Tube, in Part III Chemical Reactions in Shock Waves," Academic Press ,New York 2001 108-193 .
18. Kerr, J. A. and Parsonage, M. J.,"Evaluated Kinetic Data on Addition Reactions: Gas Phase Reactopms pf Atoms and Radicals with Alkenes, Alkynes and Aromatic Compounds. Butterworths, London .1972
19. Tsang, W., J. Amer. Chem. Soc.,107, 2783, 1985
20. Benson, S. W. "Thermochemical Kinetics" John Wiley, New York, 1974
21. Tsang, W., Walker, J.A., and Manion, J.A., Single-Pulse Shock Tube Studies on the Decomposition of 1-Pentyl Radicals, 27th International Symposium on Combustion (The Combustion Institute, Pittsburgh, PA), 135-142 (1999).
22. Tsang, W., "Pathways for the Decomposition of 1-Hexyl Radicals"; Chemical and Physical Procesess in Combustion", 1996 Fall Technical Meeting, Eastern States Section of the Combustion Institute, Hilton Head, SC., pg 515

THE STUDY OF SOOT FORMATION BY SOLID STATE NMR SPECTROSCOPY

R. J. Pugmire, M. S. Solum, Y. J. Jiang, A. F. Sarofim, J. Veranth, H.H. Schobert, P. J. Pappano**

Department of Chemical and Fuels Engineering, University of Utah, Salt Lake City, Utah 84103 and The Energy Institute*, The Pennsylvania State University, University Park, PA 16802

Introduction

Currently the Utah NMR group is using solid state NMR and ESR techniques to study the formation and structure of soot generated from various sources. These include soots made from well controlled laboratory environments using either a flat flame burner[1] or drop tube furnace, soots made in various sizes of pool fires, soots from diesel engines and soots from various other sources. The study of the formation of soot is important because of the respiratory effects associated with the inhalation of the small soot particles. These soot particles may also contain poly-aromatic hydrocarbons (PAH's) that are some of the building blocks in soot formation and some of these are known to be carcinogenic. As soots are generally very aromatic (f_a > 0.90) it is sometimes useful to compare their properties to those of anthracite coals.

Generally aerosols are generated that may be extracted with dichloromethane and the extract (tar) and residue (real soot) may be studied separately, when the amount of material permits. The extract (tar) is thought to reflect the early stages of soot formation and can be studied by 1-D NMR techniques developed to characterize coals[2] in terms of a standard set of average structural and lattice parameters. This characterization, while not providing specific compound information like gc-ms or isomer information like high resolution mass spec does, characterize the whole sample regardless of molecular weight. The residue (soot) is very often conductive and tends to give broad C-13 NMR signals. A technique has been developed[3] to characterize the extent of "graphitization" in a sample by measuring the reduction in the NMR coil Q factor and then comparing this to a standard set of diluted graphite samples to obtain a graphite-like factor. This graphite-like factor, derived from conduction electrons, tracks the carbonization of samples unlike the total unpaired electron concentration which does not. Data from aerosols made from anthracene and some anthracite coals are presented here.

Experimental

All C-13 CPMAS and single pulse (SP) NMR high speed spinning (4.1 kHz) experiments were conducted on a Chemagnetics CMX-100 NMR spectrometer with a 7.5 mm PECNCIL rotor using a procedure recently published in detail.[1] The slow spinning chemical shift measurements on anthracene aerosols were conducted on a Chemagnetics CMX-200 NMR spectrometer spinning at 501 Hz using the FIREMAT spinning sideband procedure.[4] ESR measurements were made on evacuated samples using a Bruker X-band spectrometer. Extractions were done using dichloromethane in a Soxlet extraction apparatus for 24 hrs. The graphite-like factor was determined with a Q meter as has recently been described.[3] The anthracene aerosols were made in a drop tube furnace with a 0.75 s residence time in the heated zone.

Results and Discussion

Anthracene Aerosols. Carbon-13 CPMAS spectra of three aerosols made from anthracene at temperatures of 1250 K, 1300 K and 1400 K along with the residue (soot) and extract (tar) from the extraction process of the1400 K sample are shown in Figure 1. Also shown in Figure 1 are the proton spin-lattice relaxation values and ESR unpaired spin

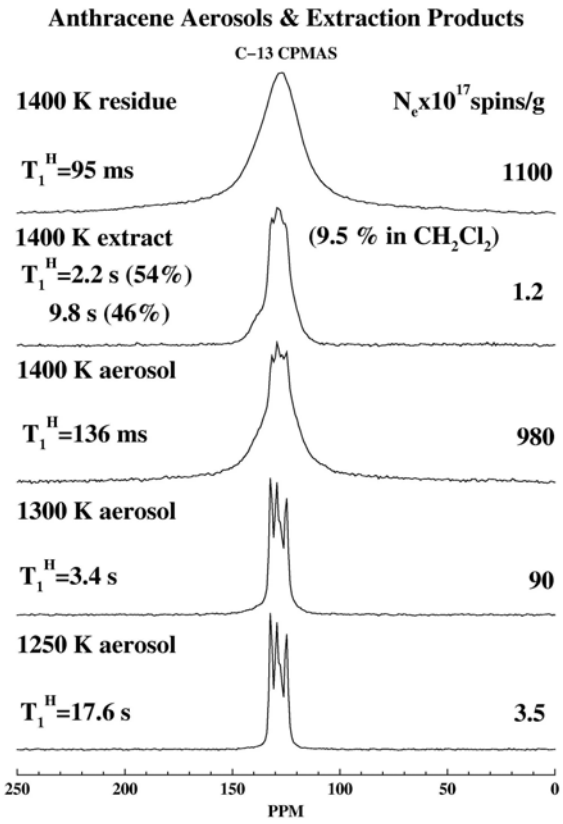

Figure 1. Carbon-13 CPMAS spectra of aerosols made from anthracene along with the extraction products from the 1400 K sample.

concentrations. The 1400 K sample had 9.5 % of the sample extracted in the soluble fraction.

The 1250 K sample shows almost unreacted anthracene, but as can be seen in Figure 1 a small amount of unpaired electrons were created providing relaxation sinks that reduced the proton T_1 value to 17.6 s so that the carbon-13 shift tensor principal values could be measured by the FIREMAT[4] spinning sideband analysis procedure. These values are shown in Table 1. The 1300 K sample gave the same values as the 1250 K sample within experimental error (1-2 ppm). This sample had a few more unpaired electrons created and a shorter T_1 of 3.4 s.

Table 1. Carbon-13 Chemical Shift Principal Values of Anthracene.

Carbon Atom	δ_{11}	δ_{22}	δ_{33}	δ_{iso}	Intensity
C-1,4,5,8	221.2	141.6	24.7	129.2	0.279
C-2,3,6,7	223.7	137.2	12.7	124.5	0.277
C-9,10	204.3	145.0	32.3	127.2	0.141
Bridgehead	210.2	192.7	-6.9	132.0	0.303

The important bridgehead tensor which can be used to give information on the size of aromatic ring systems has a δ_{33} value of -6.9 ppm that is typical of outer bridgehead carbons or cata-condensed aromatic ring systems. Values for δ_{33} in naphthalene[5] and the outer

bridgeheads in pyrene[6] give similar values of -5.9 ppm and -7 ppm respectively, while the inner bridgehead in pyrene had a value of -18 ppm.

The 1400 K sample, as can be seen in Figure1, has reacted to a much larger extent than the two lower temperature samples. Also, the unpaired electron spin count is much higher. This sample was extracted in dichloromethane and the residue (soot) and extract (tar) that comprised 9.5 % of the sample were analyzed separately. The two samples had almost three orders of magnitude of difference in unpaired electron spin count, $1.1x10^{20}$ for the residue and $1.2x10^{17}$ for the extract. The residue was very conductive giving a graphite factor[3] of 0.48 while the extract was diamagnetic with a factor of zero. The electrons in the residue are conduction electrons while the electrons in the extract are more localized. The residue of the 1400 K sample is very broad with no structure. A dipolar dephasing experiment that measures the relative amount of protonated vs nonprotonated aromatic carbon gives an aromatic cluster size of about 125 carbons per cluster if it is assumed all nonprotonated carbons are bridgeheads.[2] The broad feature of this resonance is because MAS does not completely remove anisotropic susceptibility effects.[7] A standard 1-D analysis procedure[2] of the extract gave an average cluster size of 15 carbons per cluster and there were 1.4 attachments per cluster on average. This data is consistent with anthracene molecules connected together with one or two biaryl linkages as has been seen before.[8]

Anthracite Coals. Sometimes in the study of carbonization processes it is useful to work with samples that may be better characterized or are different than soots but still with high carbon contents. Four anthracite coals from Penn State were chosen for this purpose. They are LCNN, Jeddo, UAE and Summit. NMR and other data for these samples are given in Tables 2 and 3. Carbon-13 NMR spectra of these four anthracite coals and a higher rank meta-anthracite coal and graphite are shown in Figure 2.

Table 2. Non NMR Data for the four Anthracite Coals.

Coal	%C (daf)	d_{002} (Å)	L_c (Å)	$N_e x10^{19}$ (spins/g)	ΔH_{pp} (Gauss)
LCNN $C_{100}H_{18.7}N_{1.1}S_{0.2}O_{0.8}$	95.7	3.49	59	3.26	3.76 0.04
Jeddo $C_{100}H_{22.4}N_{1.0}S_{0.2}O_{1.0}$	95.2	3.82	70	3.53	2.61 0.12
UAE $C_{100}H_{27.8}N_{0.9}S_{0.2}O_{1.8}$	94.0	3.60	85	4.90	1.24
Summit $C_{100}H_{32.0}N_{1.5}S_{0.2}O_{1.8}$	93.2	3.61	71	2.64	2.94

Table 3. NMR Data for the four Anthracite Coals.

Coal	ΔQ 100 MHz Q_0=258	G.F.	C-13 Shift (ppm)	T_{1H} (ms)	$T_{1\rho H}$ (ms)
LCNN	74	0.148	120.7	59.2	20.7
Jeddo	58	0.112	121.3	44.3	17.5
UAE	8	0.024	122.9	33.1	12.1
Summit	4	0.014	125.3	38.2	5.8

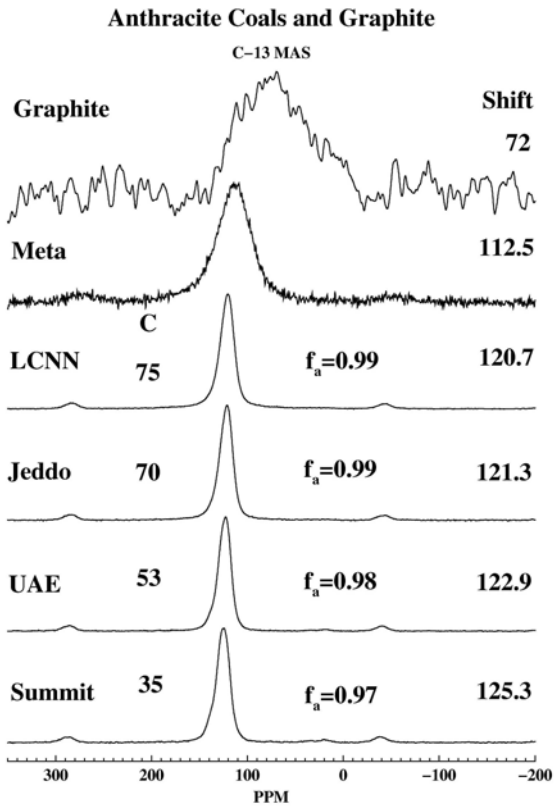

Figure 2. NMR MAS spectra of four anthracite coals (CP), a meta-anthracite coal (CP) and graphite (SP) are shown along with the aromatic cluster size, C, the aromaticity and the chemical shift of the peak.

It is interesting to note from all this data which parameters track with the carbon content and those that do not. The aromatic cluster size as shown in Figure 2, increases from 35 in the lowest carbon (Summit) sample to 75 in the highest carbon (LCNN) sample and overall correlates with the carbon content. The x-ray parameters L_c and d_{002} are scattered as a function of carbon content so no long range order correlates with the %C in these samples. Neither the total unpaired electron spin concentration or the ESR line width were found to correlate with the carbon content. The spin-lattice relaxation time T_1 that showed a correlation with the unpaired spin concentration in the anthracene samples discussed above does not correlate with the unpaired spin concentration in these coals. The correlation between the unpaired spin concentration and the proton T_1 seems to go away once all the samples have T_1's less than about 200 ms as no correlation has ever been established in coals.

The parameters that do correlate with the carbon content are the graphite-like factor that is derived from the lowering of the NMR probe Q factor, when samples start to show conductive behavior, the isotropic C-13 chemical shift and the spin-lattice relaxation in the rotating frame, $T_{1\rho H}$. These correlation's can all be explained by the increase in the size of the aromatic ring systems. In larger ring systems there is a diamagnetic shift in the δ_{33} component of the shielding tensor as was discussed above. This local effect, along with the anisotropic susceptibility effects that occur in very large extended ring systems such as graphite, also broaden the NMR resonances and give a diamagnetic shift to the NMR signals. The $T_{1\rho H}$'s correlation with carbon content can be explained as a change in the unpaired electrons from unpaired localized radicals to mobile

conduction electrons. The localized radicals are effective at shortening $T_{1\rho H}$ where the conduction electrons are not. The time dependence in the electron-nuclear interaction is probably governed by spin exchange interactions.[9]

Conclusions

It has been shown that NMR is a useful technique to study samples with different levels of carbonization. Anthracene serves as a useful model on the low end of the carbonization scale, where only a very small number of free radicals were created that shortened the relaxation time so that in a 2-D NMR experiment the shift tensors of anthracene could be measured. On the high end of the carbonization scale, where the samples become conductive, a graphite-like factor could be determined that provides a measure of the carbonization extent. On a set of four anthracite coals of varying carbon content several parameters were measured some of which correlated with the carbon content and others that did not.

Acknowledgement. This work was supported by the Department of Energy as part of the Advanced Strategic Computing Initiative (ASCI) through contract number B341493 from Lawrence Livermore National Laboratory and the DOE Fossil Energy/National Petroleum Office (FE/NPTO) contract No. DE-AC 26-99BC, and by the National Science Foundation under NSF CRAEMS grant CE 0089133.

References

(1) Solum, M. S., Sarofim, A. F., Pugmire, R. J., Fletcher, T. H., Zhang, H. *Energy Fuels*, **2001**, 15, 961.
(2) Solum, M. S.; Pugmire, R. J.; Grant, D. M. *Energy Fuels*, **1989**, 3, 187.
(3) Jiang, Y. J., Solum, M. S., Pugmire, R. J., Grant, D. M., Submitted for publication.
(4) Alderman, D. W., McGeorge, G., Hu, J. Z., Pugmire, R. J., Grant, D., M., *Molecular Physics*, **1998**, 95, 1113.
(5) Sherwood, M. H., Facelli, J. C., Alderman, D. W., Grant, D. M., *J. Am. Chem. Soc.*, **1991**, 113, 750.
(6) Carter, C. M., Alderman, D. W., Facelli, J. C., Grant, D. M., *J. Am. Chem. Soc.*, **1987**, 109, 2639.
(7) Freitas, J. C. C., Emmerich, F. G., Cernicchiaro, G. R. C., Sampaio, L. C., Bonagamba, T., *Solid State Magn. Reson.*, **2001**, 20, 61.
(8) Wornat, M. J., Sarofim, A. D., Lafleur, A. L., *24th Symposium (International) on Combustion/*The Combustion Institute, **1992**, 955.
(9) Wind, R. A., Li, L., Maciel, G. E., Wooten, J. B., *Appl. Magn. Reson.*, **1993**, 5, 161.